Measurement of Cosmic Antiprotons with the Alpha Magnetic Spectrometer aboard the International Space Station

by

Andrew Ian Chen

Submitted to the Department of Physics
in partial fulfillment of the requirements for the degree of

Doctor of Philosophy

at the

MASSACHUSETTS INSTITUTE OF TECHNOLOGY

September 2017

Author .....
Department of Physics
August 9, 2017

Certified by .....
Samuel Ting
Thomas D. Cabot Professor of Physics
Thesis Supervisor

Accepted by .....
Nergis Mavalvala
Associate Department Head of Physics

Measurement of Cosmic Antiprotons with the Alpha Magnetic Spectrometer aboard the International Space Station

by

Andrew Ian Chen

Submitted to the Department of Physics
on August 9, 2017, in partial fulfillment of the
requirements for the degree of
Doctor of Philosophy

Abstract

A precision measurement of the cosmic antiproton ($\bar{\mathrm{p}}$) flux and the antiproton-to-proton flux ratio ($\bar{\mathrm{p}}$/p) made with the Alpha Magnetic Spectrometer aboard the International Space Station is presented. The measurement covers the absolute rigidity range from 1 to 450 GV, and is based on 3.49×10^5 $\bar{\mathrm{p}}$ events and 2.42×10^9 proton (p) events. This completes the measurements of the fluxes and flux ratios for the charged elementary particles in cosmic rays by AMS. In the absolute rigidity range 60 to 500 GV, the $\bar{\mathrm{p}}$, p, and positron (e^+) fluxes are found to have nearly identical rigidity dependence. This contrasts with the electron (e^-) flux, which exhibits a different rigidity dependence. Below 60 GV, the ($\bar{\mathrm{p}}$/p), ($\bar{\mathrm{p}}/\mathrm{e}^+$), and (p/$\mathrm{e}^+$) flux ratios each reach a maximum. From 60 to 500 GV, the ($\bar{\mathrm{p}}$/p), ($\bar{\mathrm{p}}/\mathrm{e}^+$), and (p/$\mathrm{e}^+$) flux ratios show no rigidity dependence. These are new observations on the properties of charged elementary particles in cosmic rays.

Thesis Supervisor: Samuel Ting
Title: Thomas D. Cabot Professor of Physics

Acknowledgments

Thank you to Samuel Ting for inviting me on to the AMS project, for everything I have learned, and for taking the time to advise me.

Thank you to the members of the thesis committee and everyone else who helped review this manuscript. Any errors that remain are my own.

This material presented here is based upon work supported by a number of sources. Special thanks to the Laboratory for Nuclear Science Electromagnetic Interactions Group for their support under continuing Department of Energy grants, the Massachusetts Institute of Technology Henry W Kendall Fellowship, and the National Science Foundation Graduate Research Fellowship Program under Grant Number 1122374. Any opinions, findings, and conclusions or recommendations expressed in this material are those of the author and do not necessarily reflect the views of the funding agencies.

Thank you to Paolo Zuccon, Vitali Choutko, and Baosong Shan for getting me started with the enormous volume of work that is the AMS software system.

Thank you to Mike Capell for everything you have taught me about AMS and all your help along the way. To Andrey Rozhkov, Xudong Cai, Oleg Demakov, Pavel Goglov, Alexei Lebedev, and Alexandre Eline for everything you have taught me about electronics, data acquisition, computer networking, and flight operations.

Thank you to Andrei Kounine, Weiwei Xu, Zhili Weng, and Ulrich Becker for many useful conversations about physics analysis.

Thank you to my fellow graduate students who have made working on AMS so interesting: Min Xie, Wei Sun, Matthew Krafczyk, and Jie Feng.

In memory of Frederic Eppling, Alexei Chikanian, Ming-Jian Lu, and Andrey Loginov whose work we continue.

Thank you to my friends and family who have supported me on this journey. Finally, thank you Stephanie Brandt. I would have given up many times without you.

Contents

Chapter 1

Introduction and overview

The latest measurements of the antiproton flux and antiproton-to-proton flux ratio in primary cosmic rays are presented. This measurement was made using the Alpha Magnetic Spectrometer (AMS)[1] and is based on data collected aboard the International Space Station (ISS) over the four years covering 19 May 2011 – 26 May 2015. The measurement spans the absolute rigidity range from 1 to 450 GV, where rigidity (R) is defined as momentum per unit charge (p/Z). The antiproton flux and antiproton-to-proton flux ratio measurements include a total of 3.49×10^5 antiproton events and 2.42×10^9 proton events.

This thesis is presented in six chapters. This introductory chapter reviews the motivation for measuring antiprotons ($\bar{\mathrm{p}}$) in the primary cosmic rays, the propagation of cosmic rays in our galaxy, and the current physics results from AMS. Chapter 2 describes the AMS experiment—its detectors and operation. The work on the data analysis is presented in Chapter 3. Of particular importance is the correct determination of the charge sign for protons (p) and $\bar{\mathrm{p}}$ given a tracker with finite rigidity resolution. The process of determining the flux and flux ratio from the number of p and $\bar{\mathrm{p}}$ is also presented. Chapter 4 examines the systematic errors associated

[1]The magnetic spectrometer designated AMS-01 was flown aboard the Space Shuttle *Discovery* for ten days in June 1998. The flight of AMS-01 was an engineering flight that produced several physics results [1]. The magnetic spectrometer designated AMS launched 16 May 2011 aboard the Space Shuttle *Endeavour*. AMS was installed on the International Space Station 19 May 2011 and is currently in orbit. AMS is sometimes referred to in the literature as AMS-02 and AMS02. The designation AMS is used throughout this thesis.

with these measurements. This measurement of $\bar{p}$ in primary cosmic rays has unprecedented statistical precision and covers a previously unexplored rigidity range, understanding the systematic errors is the key to interpreting the results and their implications. The results from this new measurement are presented in Chapter 5. Of particular interest is the observation that the flux of $\bar{p}$ and flux of p show the same rigidity dependence. Also compared are the AMS measurements of e^+ and e^-, and the study of their respective ratios. Taken together this makes for a description of all the elementary particle fluxes and their ratios in primary[2] cosmic rays [2, 3]. These measurements, performed with the same detector, provide precise experimental information over an extended energy range in the study of elementary particles traveling through the cosmos. Finally, Chapter Six concludes with a description of the implications of these measurements and the outlook for future investigations with AMS.

1.1 A search for new physics with AMS

There are two kinds of particles traveling through the cosmos. First, neutral cosmic rays (photons and neutrinos). These can be studied in space and terrestrially for photons, and underground for neutrinos. Indeed, in the last century most of our knowledge of the cosmos has come from precise measurements of photons. Second, charged cosmic rays (e^-, e^+, $\bar{p}$, p, helium, lithium, etc.) are absorbed by the Earth's atmosphere. To study the properties of charged cosmic rays requires a precision magnetic spectrometer in space. AMS is the first large-acceptance magnetic spectrometer designed for this purpose.

The AMS magnetic field allows for separation of antimatter and matter. Furthermore, the large acceptance and sustained data taking allow for observations of rare events. Using these features, AMS is undertaking an investigation into cosmic rays

[2] In this thesis all cosmic rays of astrophysical origin are referred to as primary cosmic rays. In the literature, products of spallation in the interstellar medium are sometimes referred to as secondaries. Here secondaries refer to particles produced within the solar system: particles produced from interactions with the solar wind, in the Earth's atmosphere, or within AMS.

that probes their production, propagation, and interaction. This will deliver new insight on the limits on primordial antimatter and possible signatures of dark matter [4, 5].

1.2 Propagation of cosmic rays and production of antiprotons

AMS is able to measure cosmic rays in the energy range from hundreds of MeV to a few TeV. This is an unprecedented energy range to study primary cosmic rays which have the potential to carry information about exotic astrophysical or dark matter sources. Understanding the background sources from astrophysical cosmic ray production and propagation is required to extract this information.

Based on data from terrestrial experiments, cosmic rays are known to have energies spanning from a few eV, found in the ionized clouds of the interstellar medium, to 10^{20} eV, seen from extragalactic sources [6]. Charged cosmic rays gain their energy when they are accelerated by the changing magnetic fields of supernova shock waves. This produces a power law spectrum as described in early work by E. Fermi [7]. Work has continued on describing the spectra of cosmic rays to the present day [8–11].

The currents of accelerated particles are responsible for inducing the $\sim$0.5 nT galactic magnetic fields along which the charged particles stream [12]. Diffuse synchrotron radiation from particle trajectories bending in these fields has been observed in gamma rays [13]. Interactions with each other and the interstellar medium makes this a chaotic process. Additionally, the spallation of the particles off the interstellar medium produce antimatter in secondary cosmic rays, namely e^+ and $\bar{p}$. There is also the possibility of some heavier anti-nuclei being produced such, as antideuterons [14] and antihelium [15], but the production cross section is extremely small.

Earlier models made simplifying assumptions such as assuming a homogeneous distribution of cosmic rays and neglecting synchrotron radiation and inverse Compton scattering. Examples of such models include the leaky box model [16] and the

weighted slab model [17]. These early models were used to explain the results of early cosmic ray experiments with orders of magnitude accuracy.

1.2.1 Numerical cosmic ray propagation models

To improve on the leaky box and weighted slab models, numerical simulations are used. Current models describe cosmic ray fluxes in a more detailed way by including more parameters. This additional complexity allows the models to account for the observed structure of the Milky Way galaxy, in particular, the central bright flat disk surrounded by a massive, dimmer halo. Such multi-parameter models are known as diffusive halo models [8–11].

For example, the package GALPROP [8, 9] provides a description of the energy dependent cosmic ray fluxes for various isotopes up to nickel. This involves numerically solving transport equations with parameters that account for various cosmic ray source terms, diffusion coefficients in position space, convection, diffusive reacceleration, energy gains and losses, fragmentation, and radioactive decay. Where it is possible, empirical data is used to set parameters such as the cross sections of nuclei-nuclei interaction. There are, however, still dozens of free parameters. To restrict all these free parameters, a simultaneous analysis of all the cosmic ray particle fluxes is required.

1.3 First results from AMS

Earlier constraints on the cosmic ray particle fluxes were based on a number of measurements made by balloon based and terrestrial experiments [18–20]. Modeling predicted a falling flux of e^+, Φ^{e^+}, and a falling positron fraction, $\Phi^{e^+}/(\Phi^{e^-} + \Phi^{e^+})$. With the first results of AMS it was shown that there is an excess in the positron fraction that reaches a maximum [21, 22]. Not only that, but as seen in the e^-, e^+, and $e^- + e^+$ fluxes observed by AMS [23, 24] the excess in the fraction comes from a true excess in e^+.

Previous models had also assumed that nuclei fluxes could be described by a single

power law. This was found not to be the case with the observation with AMS of the proton flux [25] and helium flux [26].

Finally, observation by AMS of the Boron-to-Carbon flux ratio, (B/C), shows that the flux ratio follows a single power law dependence in R, for $R > 65$ GV, and that there is no structure in the ratio [27]. This is in contradiction to predictions made by many models to explain the AMS measurement of the positron fraction. In addition the observations show an exceptional agreement with the Kolmogorov theory of turbulence.

Taken together these first results of AMS show that (1) existing models cannot simultaneously explain all the high precision measurements made by AMS and (2) observations made so far with AMS are not consistent with the conventional understanding of the propagation and production of cosmic rays. This is shown in Figure 1-1. In particular, an extra source of e^+, such as annihilation of dark matter particles, is required to explain the observed flux.

1.4 Search for dark matter

Recently there have been many experiments conducting searches for dark matter [29]. Early experiments measured galactic rotation curves that indicated the existence of dark matter. More recent estimates indicate dark matter makes up ~80% of the mass in the universe [30]. These experiments measure the cosmic microwave background, the structures of galaxies, and the distribution of galaxies. Comparisons of these measurements are made to predictions from dark matter dependent models, for example the distribution of galaxies are compared to expectations from the condensation of the relativistic gases that made up the early universe [31, 32].

In addition to astrophysical phenomena such as supernova remnants [33–36], pulsars [37, 38], and collision of conventionally modeled cosmic rays [39–41], dark matter annihilation [4, 28, 42, 42–44] has been proposed as a mechanism for explaining the excess of e^+ observed by AMS. While some attempts [45] have been made to reconcile the cross section limits set by the LHC [46] and underground experiments [47] with ob-

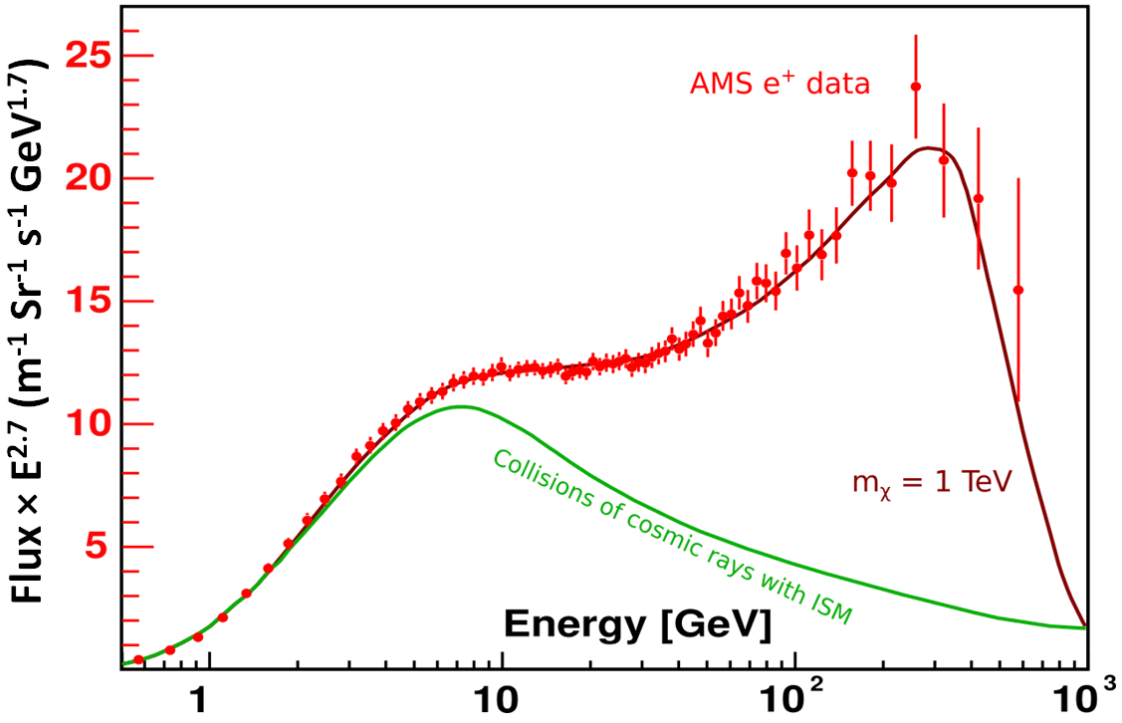

Figure 1-1: The positron flux measured by AMS [23]. Clearly the measurement is not compatible with the pre-AMS expectations based on the production of positrons by the collision of cosmic rays with the interstellar medium (ISM). An extra source term such as production from dark matter annihilation is required. Also shown here is the effect of an additional contribution from a dark matter model [28] with a dark matter candidate, χ, of mass 1 TeV.

servations of large scale structures and the AMS e^+ results [21–24], all depend heavily on models of the nature of the dark matter candidate. Given this model dependence, and the overall lack of information about the nature of dark matter, further precise measurement from these complementary search channels (annihilation, production, and scattering) is required. The complementarity of these search channels is shown by analogy in Figure 1-2.

1.5 A search using antiprotons

To enhance the power of the annihilation search channel, a measurement of all the possible products of dark matter annihilation must be made. The four charged ele-

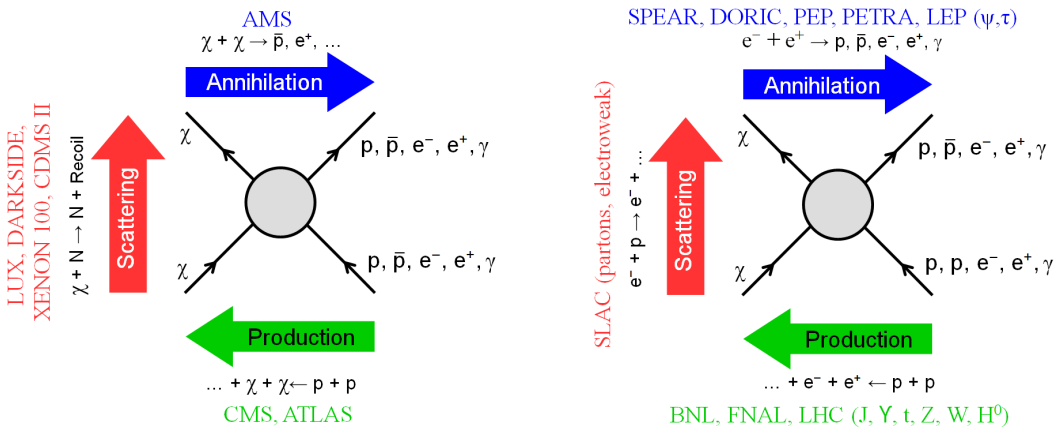

Figure 1-2: A comparison of search channels. On the left searches for a dark matter candidate, χ. Much like the physics of leptons and hadrons, different search channels are complementary and have different sensitivities. On the right a diagram representing the success of the Standard Model of particle physics. Studying the physics of leptons and hadrons—by a number of experiments—lead to discoveries (examples shown in parentheses). This allowed for the full development of the Standard Model of particle physics, with the most recent Standard Model observations including the 2012 discovery of the Higgs boson, H^0 [48, 49].

mentary particles in cosmic rays with infinite lifetime—e^-, e^+, p, and $\bar{p}$—are produced in most dark matter models [50]. Through hadronization $\bar{p}$ are produced by dark matter annhilation, but their production from alternative astrophysical sources is limited [34]. This makes the $\bar{p}$ flux an important tool for separating different theories on the origin of the e^+ excess already observed by AMS.

Indeed, since the first observations of $\bar{p}$ in cosmic rays [51, 52], many studies have been performed [1, 53–64]. These studies on the $\bar{p}$ flux and the $\bar{p}/p$ flux ratio are limited due to the $\sim 10^4$ times abundance of p compared to $\bar{p}$. Using AMS and the analysis presented in this thesis, a separation power of $\sim 10^6$ is achieved. This allows for the percent level accuracy needed for sensitivity of $\bar{p}$ to cosmic phenomena [65–68, 68–74].

Chapter 2

The AMS detector

A full description of the AMS detector is presented in References [75–79]. All of the detector elements are used for particle identification in the present analysis. These elements consist of the silicon tracker [80, 81], the permanent magnet [1], the time of flight counters (TOF) [82, 83], the anticoincidence counters (ACC) [83, 84], the transition radiation detector (TRD) [85], the ring imaging Čerenkov detector (RICH) [86], and the electromagnetic calorimeter (ECAL) [87]. A schematic diagram of the AMS experiment is shown in Figure 2-1.

2.1 Silicon tracker

AMS performs its magnetic spectroscopy using a nine layer silicon tracker and a cylindrical permanent magnet. The silicon tracker records the position of charged particles crossing its 2264 double-sided silicon micro-strip sensors. From these positions, the bending of charged particles in the magnetic field is extracted. The natural unit described by this bending is R. This is also the natural unit for charged particles propagating in galactic magnetic fields. Since R is the natural unit for AMS and for charged cosmic rays, dependence on R (expressed in volts) is primarily used in this thesis, rather than energy (expressed in eV) as is common in other particle physics experiments.

The nine layers of the silicon tracker are referred to by the designations L1–L9.

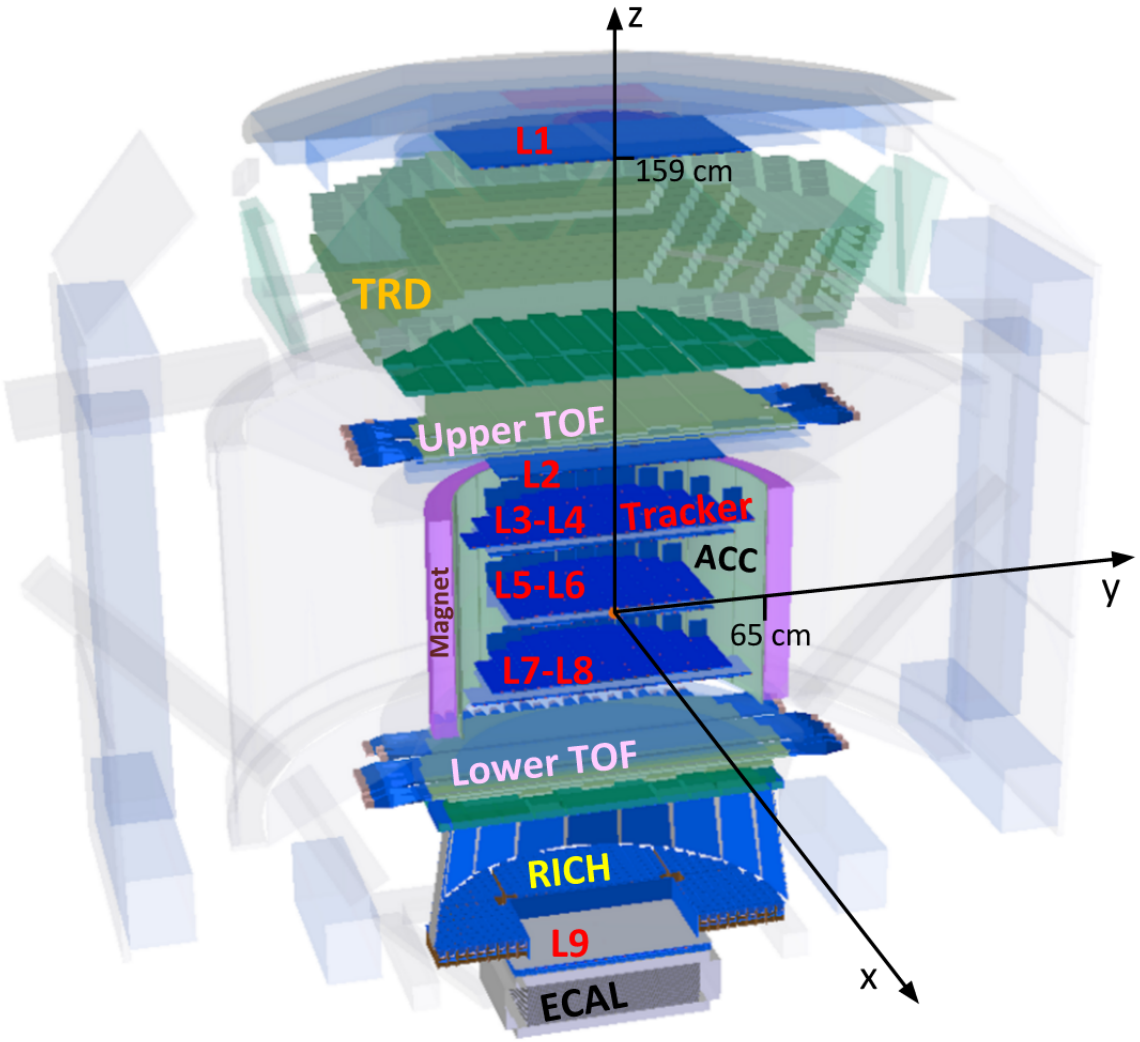

Figure 2-1: A schematic view of AMS. Labels correspond to the abbreviated detector names and individual tracker planes. The origin of the AMS coordinate system is centered at the center of the magnet bore. This rendering is generated from the geometry used in the comprehensive simulation of AMS described in Section 3.4. Active detector elements are shaded, while support structure is partially transparent.

L1 is at the top of AMS. The inner tracker is defined as the layers L2–L8. L9 sits above the ECAL. The total span from L1–L9 is 2.95 m.

The coordinate system used for this analysis is centered at the center of the inner tracker. The z-axis is defined to be along the cylindrical axis of the magnet bore, and the x-axis is defined to point in the direction of the magnetic field. This means that particle trajectories bend in the y–z plane.

2.1.1 Permanent magnet

In the study of antimatter, the permanent magnet surrounding the inner tracker is crucial since the ability to measure the charge sign is required.

The dipole magnetic field is produced by an array of 64 magnetic sections arranged cylindrically. These sections are composed of 100 blocks of magnetized NdFeB and stacked to form the $\sim$1 m tall central core of AMS. Together these arrays produce a dipole magnetic field with 1% level uniformity and 0.15 T intensity. A temperature-corrected map of the magnetic field is used for the full track fitting and reconstruction.

2.1.2 Tracker reconstruction

A full description of the track reconstruction and fitting of resulting reconstructed rigidities is given in reference [88]. To summarize, the time stability and absolute alignment of the AMS tracker is established using an infrared laser system and high energy proton data, respectively [25]. The signal amplitudes are read out from every fourth strip on the p-side and every other strip on the n-side. Clusters are then associated with the signal amplitudes and fitted, taking into account the capacitive coupling between strips. This determines a partially degenerate position for the cluster. Clusters that match a three dimensional track hypothesis for various layer permutations are assigned to tracker track candidates. This matching also includes hits in the TOF. The track finding efficiency is estimated to be 90% to 95% for singly charged particles [89].

The corresponding rigidity of a track is fit using the algorithm specified in Reference [90]. The fit corresponds to a path integral fit over the expected trajectory given the Lorentz force on the charged particle traversing the magnetic field. Multiple scattering and energy loss are allowed for when determining the most probable reconstructed R.

2.1.3 Rigidity resolution

The coordinate resolution for $|Z| = 1$ particles in the silicon tracker is $\sim$10 μm in the y direction [91]. This resolution is consistent with the first-principles estimate of the resolution given a pitch width of 27.5 μm [80] in the y direction. Given the magnetic field strength B, and the span L, the expected resolution is $\propto 1/(BL^2)$. For this coordinate resolution, B, and L, the maximum detectable rigidity (MDR) is 2 TV for $|Z| = 1$ particles, where MDR is defined as the rigidity at which there is a 1-σ chance R is assigned the wrong charge sign.

2.2 Time of flight counters

The TOF is constructed of four layers of plastic scintillator paddles and provides the primary trigger for AMS. The timing information from the four layers also provides a measurement of velocity with a resolution of $\Delta\beta/\beta^2 = 4\%$ for |Z| = 1 and vetoes upward going particles. The signal amplitude corresponding to energy deposition from passing particles provides a measurement of charge.

2.3 Transition radiation detector

The TRD identifies transition radiation produced by highly relativistic particles crossing through the fleece radiators in each of its 20 layers. The energy deposition from ionization and transition radiation is amplified and read out by 6 mm diameter proportional tubes. In this analysis, e^- in the energy range 1–500 GeV and high energy p are identified as primary backgrounds to $\bar{p}$ identification. The TRD plays a key role selecting these backgrounds since the e^- and p that contribute are highly relativistic, with Lorentz factors $\gamma > 1000$, making the production of transition radiation more likely.

2.3.1 TRD likelihood estimator

To separate $\bar{\mathrm{p}}$ and p from e^- and e^+ events, an estimator constructed from the ratio of the log-likelihood probability of the $\mathrm{e}^\pm$ hypothesis to that of the $\bar{\mathrm{p}}$ or p hypothesis in each layer is used. This estimator, Λ_{TRD}, is described in [21]. The estimator is constructed such that $\bar{\mathrm{p}}$ and p have $\Lambda_{\mathrm{TRD}} \approx 1$, and are efficiently separated from $\mathrm{e}^\pm$, which have $\Lambda_{\mathrm{TRD}} \approx 0.5$.

2.4 Ring imaging Čerenkov detector

The RICH provides an additional velocity measurement based on the opening angle of the Čerenkov radiation cone produced by charged particles passing through the the aerogel or NaF radiators. The RICH has a velocity resolution $\Delta\beta/\beta = 0.1\%$ for $|\mathrm{Z}| = 1$. This ensures separation of $\bar{\mathrm{p}}$ and p from light particles ($\mathrm{e}^\pm$ and $\pi^\pm$) below 10 GV.

2.5 Electromagnetic calorimeter

The ECAL measures the three dimensional shower passing through its interleaved, 17 X_0, lead foil and scintillating fiber volume. The energy resolution of the ECAL for $\mathrm{e}^\pm$ data was found to be $\sigma(E)/E = (10.4 \pm 0.2)/\sqrt{E[\mathrm{GeV}]} \oplus (1.4 \pm 0.1)\%$ with linearity better than 1% for $E < 300$ GeV as observed in test beam data.

2.5.1 ECAL BDT

The ECAL is also used to separate $\bar{\mathrm{p}}$ and p from $\mathrm{e}^\pm$. In the ECAL, $\mathrm{e}^\pm$ create electromagnetic showers while $\bar{\mathrm{p}}$ and p produce hadronic showers. The characteristic length scale for energy loss in electromagnetic showers is the radiation length, X_0. For the AMS ECAL $X_0 = 9.76$ mm. The characteristic length scale for hadronic showers is the nuclear interaction length, 29.4 cm for the AMS ECAL. Additionally, hadronic showers are highly variable.

The recorded three dimensional showers are compared based on 19 variables such as the energy weighted average depth of the shower, the shower maximum, the shower width, and the fraction of energy deposited in each layer. This comparison is done using a boosted decision tree method (BDT) [92]. The method is further described in Section 3.2.1. The BDT classifier is normalized such that hadronic showers have a $\Lambda_{\mathrm{ECAL}} \approx 1$, and electromagnetic showers have $\Lambda_{\mathrm{ECAL}} \approx -1$.

2.6 Anti-coincidence counters

The ACC consist of 16 plastic scintillating paddles surrounding the inner tracker. The ACC have a 0.99999 efficiency at rejecting cosmic rays entering the inner tracker from the side. Additionally, the ACC are used to discriminate possible p backgrounds from the $\bar{\mathrm{p}}$ signal. This discrimination is based on comparing the expected number of ACC paddles hit by low energy secondaries to expectations based on the energy of the incoming p or $\bar{\mathrm{p}}$. These low energy secondaries mostly correspond to upward going particles created when high energy particles interact inelastically with the ECAL, a phenomenon known as backsplash. The amount of backsplash is energy dependent. For $E > 200$ GeV, 60% of p create a hit in at least two paddles.

2.7 Operation of the AMS detector

The detectors that make up AMS generate ∼10 Mbits/s of data at an average trigger rate of 1 kHz. This is an exceptional data rate for an instrument operating in orbit. In addition to the inherent challenges associated with operating a high bandwidth experiment, AMS must cope with the constantly changing environmental conditions experienced aboard the ISS. AMS is able to maintain the multi-year high-uptime operation shown in Figure 2-2 through constant monitoring and real time responses to changing conditions.

Changing conditions vary in time scales. AMS experiences full day-night thermal cycles during the 93 minute period of the ISS orbit. Additionally, corrections on the

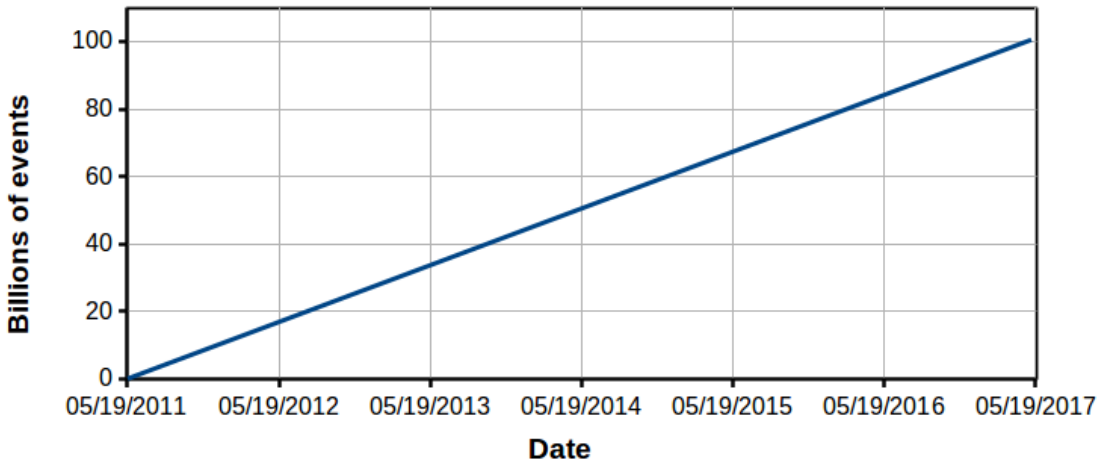

Figure 2-2: The data acquisition rate observed by AMS. AMS is able to achieve near constant uptime over multiple years through constant monitoring and rapid response to changing conditions. On 8 May 2017 AMS reached 100 billion observed events.

absolute alignment of AMS must account for the changes in solar beta angle which have time scales of roughly a month. Finally, there are multi-year changes from reduction–oxidation reactions on exposed surfaces.

During special operations of the ISS, such as a visiting vehicle docking or robotic arm manoeuvres, extra material can enter the AMS field of view. Such periods total a few dozen hours over five years and are monitored in real time. Data collected during these times are subsequently excluded from samples considered for physics analysis.

2.7.1 Data acquisition and transfer

The data taken by AMS are recorded in individual units known as events. These events represent a single set of readouts from the two hundred thousand front end channels of the AMS detectors. The number of events AMS has recorded and reconstructed is shown in Figure 2-2.

The readout is triggered at two levels. The first level is the fast trigger which relies on signals from the TOF, ACC, and ECAL. While this trigger is also induced by high-Z signals or electromagnetic showers, for this analysis the general charged particle trigger provided by the TOF is used.

The next level trigger is processed by the dedicated level-one electronics referred to as JLV1. Of the fourteen trigger permutations accepted by the level-one trigger this analysis focuses on two. (1) The charged particle trigger. This requires a threshold in the TOF signals consistent with $|Z| \geq 1$ on all four TOF planes and no veto from the ACC. This represents the vast majority of triggers accepted and recorded as events. (2) The unbiased charged particle trigger. This unbiased trigger requires only three of four TOF planes, and provides a near 100% efficiency reference to determine trigger efficiencies. It is pre-scaled by a factor of 100, since it is used to compute efficiencies of the dedicated physics triggers.

When a signal is accepted by the level-one trigger, the analog signal from the front-end electronics are read out and digitized by hundreds of digital signal processors (DSP). These signals are also compressed primarily through pedestal subtraction and zero suppression. This allows for more data to be stored aboard the 112 GB flash memory of the AMS main data computer (JMDC) or the dedicated laptop inside the ISS. The 1:3000 compression also makes near real-time data transmission through the Tracking and Data Relay Satellite System manageable. This transmission is done on the K_U band spanning 12–18 GHz. Real time commanding and monitoring are done on the S band spanning 2–4 GHz.

2.7.2 Further considerations aboard the ISS

In addition to the environmental conditions faced by AMS aboard the ISS, the Earth and Sun both produce magnetic fields that affect the particles observed by AMS. The effect of solar modulation on the $\bar{p}$ flux will be published separately. Of particular interest will be observations on the full 11 year period of the solar cycle.

The Earth's magnetosphere does, however, affect both the operation of AMS and the physics analysis presented here. The dipole component of Earth's magnetic field is inclined at 11° and offset by 500 km with respect to the Earth's rotational axis. When combined with the 52° orbital inclination and 400 km orbital altitude of the ISS, AMS passes through regions of varying magnetic field intensities. Additionally the distribution of magnetic field intensities varies from orbit to orbit.

Spallation of cosmic rays with the Earth's atmosphere can create particles with trajectories that trap them in a magnetic mirror formed by the Earth's magnetosphere [93]. This creates what are called the Van Allen radiation belts. The region where the inner Van Allen radiation belt crosses low Earth orbit has a field strength of $\sim$23 μT. The concentration of charged particles increases by an order of magnitude, but most of these have MeV energies below the AMS trigger threshold. This area is known as the South Atlantic Anomaly (SAA), and AMS sees nearly a four times increase in trigger rate. Some $\bar{\text{p}}$ have been observed in the SAA, but these are spallation products [94]. Trapped $\bar{\text{p}}$ are not included in this analysis, since they are not primary cosmic rays.

To cope with the highly ionizing environment, especially in the SAA, the AMS electronics are designed to be radiation resistant and highly resilient. This includes a memory self-test for the DSPs which are corrected by an automatic procedure, or as necessary, manual intervention.

The SAA is excluded from the analysis presented in this thesis. This is done by requiring a detector "livetime" $> 50\%$. This cut is consistent with geometrical cuts on the SAA, but is more refined as the SAA has a boundary that moves with time and altitude.

The livetime is analogous to duty cycle, but in the case of the SAA, AMS observes a rise in trigger frequency, whereas duty cycle is typically expressed in terms of constant operating frequency. With a constant readout and processing time totaling 600 μs, live time drops off dramatically in the SAA.

The effects of geomagnetically trapped particles not in the SAA contributing to observed $\bar{\text{p}}$ counts are discussed in 4.1.1.

2.7.3 Calibration and test beam

In addition to operating aboard the ISS, AMS took data samples on the ground. These include samples taken in August 2010 at the CERN Super Proton Synchrotron (SPS), as well as muon air shower data. High energy proton data of 180 and 400 GeV were taken at 1,650 locations and orientations. This test beam data is critical

for calibrating the absolute rigidity scale of the tracker rigidity reconstruction and determination of the tracker rigidity resolution function.

Additional samples of $e^{\pm}$ up to 290 GeV were taken to test the TRD and ECAL performance. Samples of π up to 180 GeV verify TRD performance up to $\gamma = 1.3 \times 10^4$, equivalent to 1.2 TeV for p data.

Chapter 3

Data analysis

The task now is to use the AMS detector as described in Chapter 2 to make a measurement that can contribute new insight to the physics goals identified in Chapter 1. To achieve this, the measurement of the $\bar{p}$ flux is presented. This measurement completes the precise measurement of elementary particle fluxes in primary cosmic rays (p, e^-, $\bar{p}$, and e^+). The simultaneous measurement of the $\bar{p}/p$ flux ratio allows for reduced systematic errors compared to the fluxes alone.

Data analysis is performed in 57 absolute rigidity bins. The same binning as the AMS p flux measurement [25] is chosen below 80.5 GV. Above 80.5 GV, two to four bins from [25] are combined to ensure sufficient $\bar{p}$ statistics.

3.1 Event selection

The first step in the $\bar{p}$ flux and $\bar{p}/p$ flux ratio measurements is making a selection to determine the number of $\bar{p}$ observed by AMS. This selection is from the over 65 billion cosmic ray events recorded in the first 48 months of AMS operations. A $\bar{p}$ candidate made with this selection is shown in Figure 3-1, identification as a $\bar{p}$ is made with tools developed for this analysis.

Only events collected during normal detector operating conditions are used in this analysis. This includes selecting only time periods when the AMS z-axis is pointing within 40° of the local zenith. Intervals when the ISS is in the SAA are excluded.

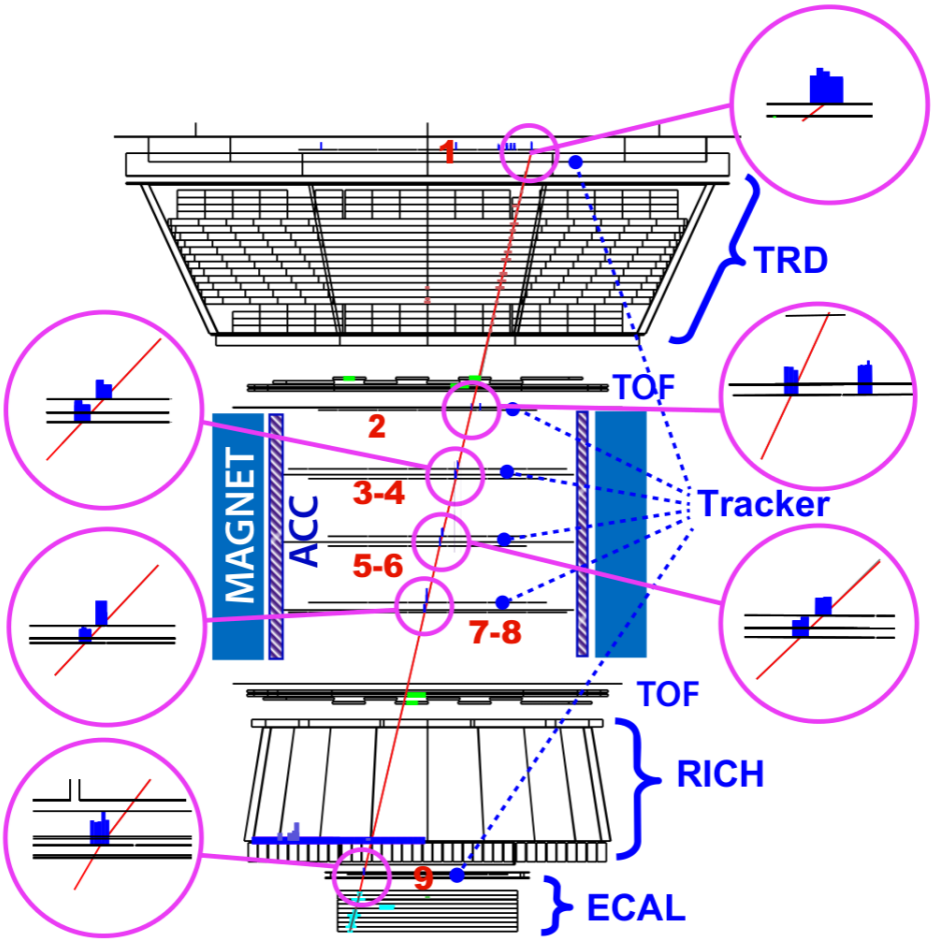

Figure 3-1: The AMS event display showing the bending projection of an antiproton event. The reconstructed particle trajectory is shown in red. In the insets the close matching of the track to the pulse heights measured in each layer of the tracker is shown. This event is identified as a likely $\bar{\text{p}}$ with all the subdetector elements of AMS. The particle is identified as downward-going with charge $|Z| = 1$. The best fit for the reconstructed rigidity from the nine tracker layers is $R = -435$ GV. Finally, the particle is hadronic and correctly charge sign identified with $\Lambda_{\text{TRD}} = 0.908$ and $\Lambda_{\text{CC}} = 0.983$.

A further selection requires events with one track in the inner tracker and a matching track in the TRD is made. Particles must have a measured velocity $\beta > 0.3$ in the TOF corresponding to a downward-going particle.

To maximize the statistical power of the measurement while simultaneously maximizing the accuracy of the rigidity measurement, the analysis requires different selections on the external tracker layers for different rigidities. This allows the largest

acceptance for the low rigidity $\bar{\text{p}}$ flux and then brings in the longer lever arm of external tracker layers to measure $\bar{\text{p}}$ at high rigidity. Only inner tracker layers are required below 38.9 GV. From 38.9 to 147 GV, either L1 or L9 is required. From 147 to 175 GV, L9 is required. Above 175 GV, both L1 and L9 are required.

In order to maximize the accuracy of the rigidity measurement, the reconstructed track is required to fit with a χ^2/d.o.f. < 10 in both the bending and nonbending projections. The dE/dx measurements in the TRD, the TOF, and the inner tracker must be consistent with $|Z| = 1$.

To select only primary cosmic rays, the reconstructed track rigidity is required to exceed the maximum geomagnetic cutoff by a factor of 1.2 for both positive or negative $|Z| = 1$ particles. The cutoff is calculated by backtracing [25, 95] using the most recent IGRF geomagnetic model [96, 97]. This backtracing is performed by numerical integration of the particle trajectory along the modeled geomagnetic field up to 50 Earth radii. The effects of backtracing are further discussed in Section 4.1.1.

Events satisfying the selection criteria are classified into two categories: (1) positive and (2) negative rigidity samples.

A total of 2.42×10^9 events with positive rigidity are selected as p. This sample is 99.9% pure p with almost no background, since p make up the vast majority of $Z = +1$ particles in cosmic rays. Deuterons are not distinguished from p, their contribution decreases with rigidity. At 1 GV the contribution from deuterons is less than 2% and at 20 GV it is 0.6% [1, 98]. The effective acceptance of this selection for p is significantly larger than in Reference [25]. This is is a result of the less strict requirements on the tracker layers L1 and L9. This leads to a much larger field of view at low rigidities and, therefore, to a significant increase in the number of p observed.

The negative rigidity event category contains both $\bar{\text{p}}$ and several background sources: e^-, light negative mesons (π^- and a negligible amount of K^-), and p that have been reconstructed with the wrong charge sign.

The light mesons are produced in the interactions of primary cosmic rays with the detector materials.

There are p reconstructed with the wrong charge sign charge due to scattering

within AMS, production of secondaries, and finite rigidity resolution. These are referred to as charge confusion protons.

The contributions of the different background sources vary with rigidity. For example, light negative mesons are present only at rigidities below 10 GV, whereas charge confusion becomes noticeable only at high rigidities ($R > 150$ GV). Electron background is present at all rigidities.

3.2 Identification of charge confusion protons

Since the charge confusion p are a primary source of background at the previously unexplored high energies covered by this analysis, a dedicated estimator using the BDT technique [92] is developed. The estimator, referred to as Λ_{CC}, efficiently separates charge confusion p from $\bar{\mathrm{p}}$.

This BDT-based classifier was cross checked extensively to ensure good performance and minimal bias. One such cross check was the independent construction of a classifier using a negative log-likelihood ratio test. This classifier is based on a multiple Gaussian approximation of the tracker hit resolution function. For the full analysis, the BDT based classifier is used as it does not necessitate assuming resolution functions and allows for the incorporation of information from multiple detectors.

Validation of Λ_{CC} is also performed by comparing the performance of Λ_{CC} to the $\mathrm{e}^{\pm}$ charge confusion estimator. The $\mathrm{e}^{\pm}$ charge confusion estimator is similarly designed, but benefits from the ability to do energy–momentum (E/p) matching. Since $\mathrm{e}^{\pm}$ produce electromagnetic showers in the AMS ECAL, their energy is reconstructed independently of the rigidity measurement.

The BDT for Λ_{CC} combines information from the tracker such as the track χ^2/d.o.f., best fit rigidity reconstructions with different combinations of tracker layers, and the number of hits in the vicinity of the track. It also includes the charge measurements in the TOF and the tracker. These charge measurements are effectively dE/dx measurements, therefore they help to identify events with secondaries which can deposit

additional energy near the primary particle track.

With this method, $\bar{p}$, which have $\Lambda_{CC} \approx +1$, are separated from charge confusion p, which have $\Lambda_{CC} \approx -1$. The performance of Λ_{CC} above 100 GV is shown in Figure 3-2.

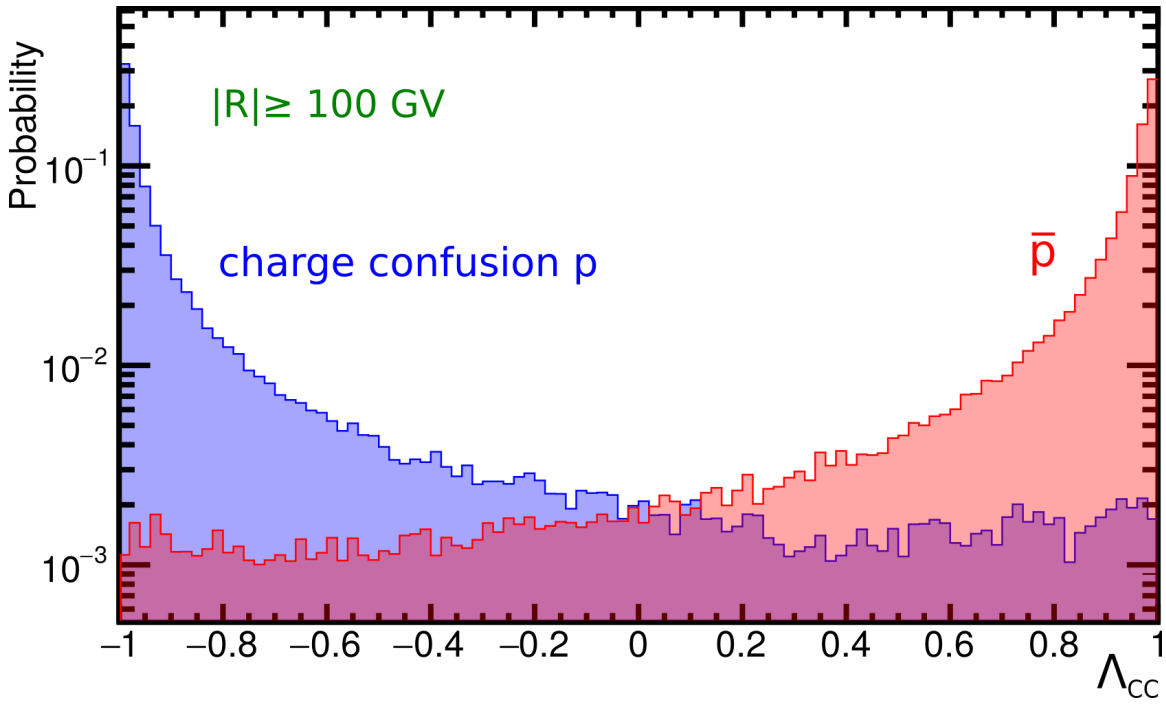

Figure 3-2: The performance of the boosted decision trees based charge confusion estimator Λ_{CC}. This plot shows the clear separation based on a power law scaled Monte Carlo simulation sample of p and $\bar{p}$ events in AMS. The charge confusion p are shown in blue, while the $\bar{p}$ are shown in red. Clearly the distributions are sharply peaked with $\Lambda_{CC} \approx +1$ for $\bar{p}$ and $\Lambda_{CC} \approx -1$ for charge confusion p. The small component of charge confusion p that is not separated represents an irreducible background for this analysis. They are accounted for using a template fitting technique, with the corresponding errors carried through the analysis.

3.2.1 The boosted decision tree method

The BDT technique [92] was selected for Λ_{CC} as it is has several advantages in this application, such as straightforward interpretation, little tuning, good performance in training and classification, and resistance to overtraining [99].

The boosted decision trees are composed of an ensemble of decision trees. These decision trees are made of a series of nodes where a candidate event is compared

to the background (charge confusion p) and signal ($\bar{\text{p}}$) hypotheses using one of the variables described above. At the end, the final nodes of the tree are called leaves and correspond to a decision, either p or $\bar{\text{p}}$ in this case. The boosting corresponds to selecting the best-performing trees from the generated ensemble of trees and weighting their votes on the classification of the candidate event.

For Λ_{CC} an ensemble of trees is generated for each rigidity bin. Boosting using the gradient boosting method weights the votes of 400 selected trees, with each tree using a three node depth.

The training samples are based on the AMS Monte Carlo simulation described in Section 3.4 as well as the 400 GeV p test beam data. The training sets the cutoffs for the nodes and weights for the boosting. Performance is classified by the Gini index metric [99]. Training and performance samples are separated by even and odd event number.

3.3 Template fitting

Now that the tools to separate signal from background have been developed, the total number of each type can be extracted for the negative R sample. To do this, information from the TRD, TOF, tracker, RICH, and ECAL are combined using a template fitting technique. This allows for the most precise determination of the relative contributions to the sample, as opposed to cuts where there is a trade-off between efficiency and rejection power.

The template fitting technique uses signal and background templates for each bin. The normalizations of the signal and background templates are varied to fit the data sample. The fit gives the quoted observed number of $\bar{\text{p}}$ signal events and the statistical errors. The distribution of the variables for the template definitions are the same for $\bar{\text{p}}$ and p if they are both reconstructed with a correct charge-sign. This similarity has been verified with the Monte Carlo simulation (Section 3.4) and the $\bar{\text{p}}$ and p data for $2.97 \leq |R| < 18.0$ GV.

Thus the signal template is always defined using the high-statistics p data sample.

This minimizes the error from the signal template shape. Three overlapping rigidity regions with different types of template functions are defined to maximize the different resolving power of the AMS detectors for this analysis. These are (1) the low absolute rigidity region (1.00 – 4.02 GV), (2) the intermediate absolute rigidity region (2.97 – 18.0 GV), and (3) the high absolute rigidity region (16.6 – 450 GV). In the overlapping rigidity bins the results are compatible within systematic errors. The results with the smallest error are presented.

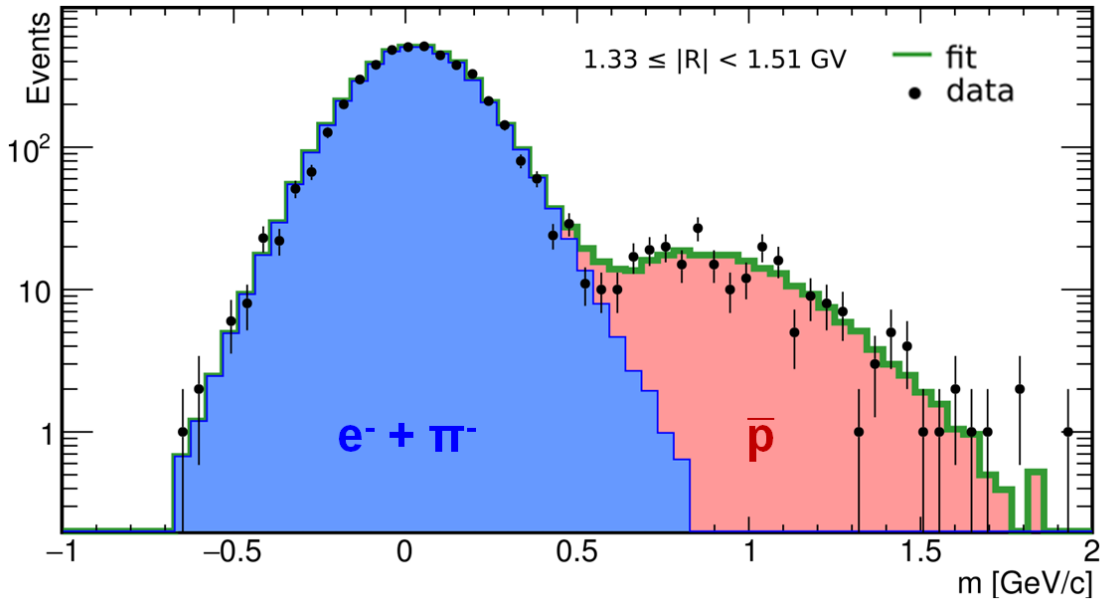

Figure 3-3: The one dimensional template fit along the reconstructed mass distribution of the low absolute rigidity sample. Shown here is the fit to the negative rigidity sample for $1.33 \leq |R| < 1.51$ GV. The $\bar{p}$ and light particle templates are constructed using the TRD, RICH, and ECAL. The numbers of signal and background events are determined by varying the normalization of the templates and fitting to data.

3.3.1 The low rigidity region (1.00 – 4.02 GV)

At low rigidities the template fit is performed using a background template for e^- and π^- defined from the data. The data sample used to create the template is selected using Λ_{TRD} and the RICH. The ECAL is used to select a nearly pure background sample for events within the ECAL acceptance. This sample is used to verify the template shape.

The fit is then performed along according to mass distribution, calculated from the rigidity measurement in the inner tracker and the velocity measured by the TOF as $m = |R|/(c \times \beta_{TOF})$. The one dimensional fit along the reconstructed mass distribution axis is shown in Figure 3-3.

3.3.2 The intermediate rigidity region (2.97 – 18.0 GV)

At intermediate rigidities, Λ_{TRD} and the velocity measured with the RICH are used to separate the $\bar{\mathrm{p}}$ signal from light particles. As an example, Figure 3-4 shows that the $\bar{\mathrm{p}}$ signal and the background are well separated in the $[\beta_{RICH} - (\mathrm{sign}(R) \times \Lambda_{TRD})]$ plane for the absolute rigidity range 5.4-6.5 GV.

To determine the number of $\bar{\mathrm{p}}$ signal events, the π^- background is removed by a rigidity dependent β_{RICH} cut and the Λ_{TRD} distribution is used to construct the templates and to differentiate between the $\bar{\mathrm{p}}$ signal and e^- background. The background template is defined from the e^- data sample selected using ECAL. The Monte Carlo simulation matches the data for e^- events inside the ECAL. The Monte Carlo simulation was then used to verify that the e^- template shape outside the ECAL and inside the ECAL are identical.

3.3.3 The high rigidity region (16.6 – 450 GV)

In the high rigidity region, the two-dimensional [Λ_{TRD}–Λ_{CC}] distribution is used to determine the number of $\bar{\mathrm{p}}$ signal events. The lower bound of Λ_{CC} is chosen for each bin to optimize the accuracy of the fit. For example, for $|R| > 175$ GV, the region with $\Lambda_{\mathrm{CC}} \geq -0.6$ was chosen. Variation of the lower bound is included in the systematic errors discussed in Chapter 4.

To fit the data, three template shapes are defined. The first two are for $\bar{\mathrm{p}}$ and e^- with correctly reconstructed charge sign and the last one is for charge confusion p.

An example of the fit to the data is shown in Figure 3-5 for the rigidity bin 175-211 GV. The distribution of data in the [Λ_{TRD}–Λ_{CC}] plane is shown in the left panel and the fit results showing the signal and background distributions is shown in the

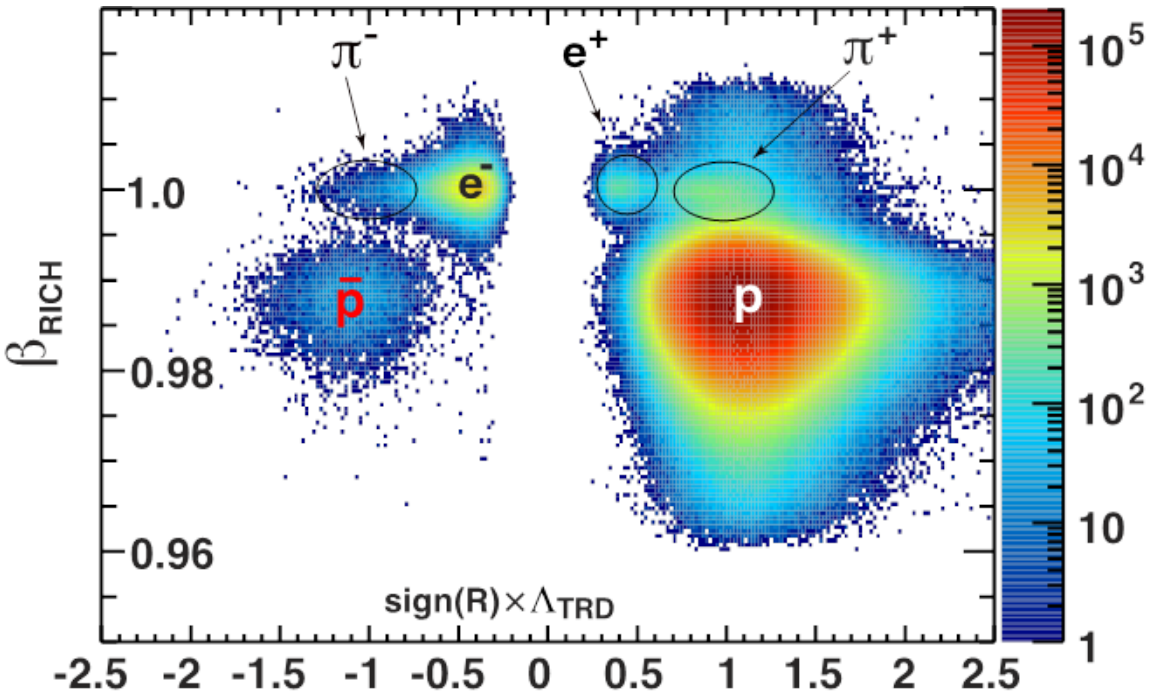

Figure 3-4: Particle identification at intermediate rigidities. Shown here are negative rigidity and positive rigidity data samples in the $[\beta_{RICH} - (\text{sign}(R) \times \Lambda_{TRD})]$ plane. The samples correspond to the $5.4 \leq |R| < 6.5$ GV rigidity bin. The contributions of $\bar{\text{p}}$, p, e^+, e^-, π^+, and π^- are clearly seen. The $\bar{\text{p}}$ signal is separated from the backgrounds by a rigidity dependent β_{RICH} cut to make templates for fitting.

right panel. The χ^2/d.o.f. of the fit is 138 for 154 degrees of freedom. The χ^2/d.o.f. does not account for correlation between bins and the covariance between the two classifiers.

3.4 The AMS Monte Carlo simulation

As much as possible, this analysis is designed to be data-driven. This limits the biases and uncertainties associated with model-dependent simulation. For example, the multiple independent detectors that make up AMS are used to construct the templates in the low and intermediate regions. In all rigidity regions the correct charge sign p sample is used to define the correct charge sign $\bar{\text{p}}$ template. The e^- high rigidity region template was likewise verified with a high purity ISS data sample selected with Λ_{ECAL}. This leaves the high rigidity region charge confusion p

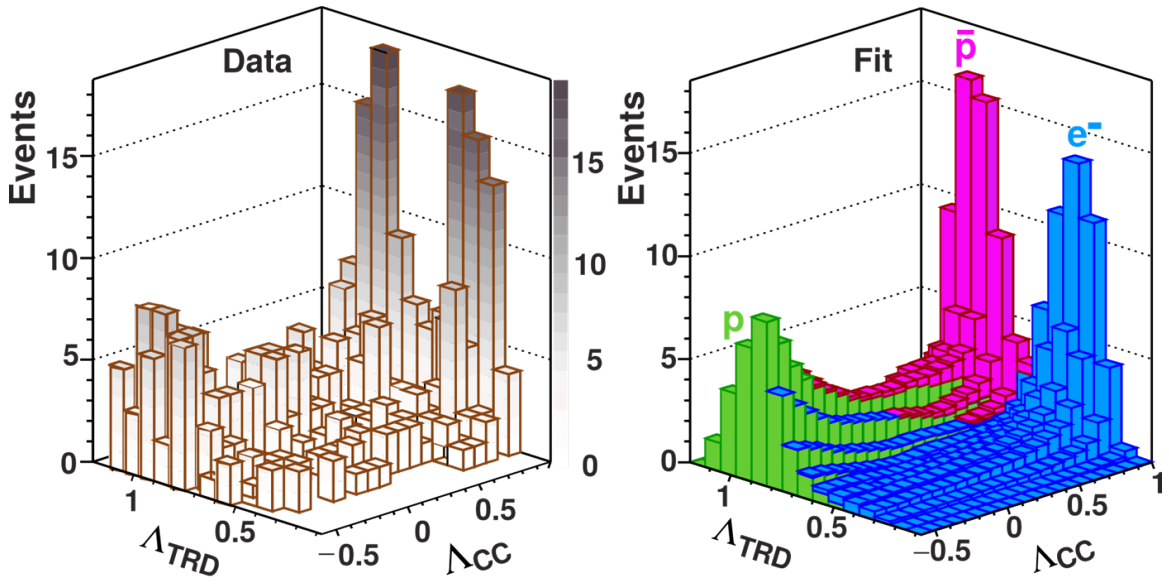

Figure 3-5: A two dimensional fit to the number of antiprotons. On the left, the distribution of data events in the negative rigidity sample. This corresponds to the $175 \leq |R| < 211$ GV rigidity bin. On the right, the template fit to the data with χ^2/d.o.f. = 138/154. There are three templates used in the fit: $\bar{p}$ signal template, the e^- background template, and the charge confusion p background template.

background as the last set of events to address.

As mentioned above, Λ_{CC} was trained on simulated events. Also, the two-dimensional template in the $[\Lambda_{TRD} - \Lambda_{CC}]$ plane is based on the shape of charge confusion p generated in the AMS Monte Carlo simulation. A number of studies are made to account for any of the systematic errors introduced by this method. This is discussed in Chapter 4.

The AMS Monte Carlo simulation used in this analysis is based on the GEANT 4.10.1 package [100, 101]. The generated events are scaled to the power law fluxes observed by AMS [25] and generated isotropically from a plane covering the AMS field of view. Properties of the incoming particle and particles produced from interactions within AMS are recorded as they propagate and further interact. The detailed model of AMS used for the simulation is shown in Figure 2-1. After simulating the interaction, digitization, and electronics readout, the simulated events are reconstructed with the main AMS reconstruction software [102] in the same way as data collected on the ISS and during the test beam.

Additionally, several steps are taken to verify the fidelity of the AMS simulation. The physics models used in the simulation were varied by their cross section uncertainties as well as against various sets of models. This includes comparisons between the default GEANT4 hadronic interaction models and the so called dual parton model (DPMJET) [103].

Finally, comparisons between data and simulation are made from the overall classifier performance down to the individual resolution functions of the AMS detectors. To check the performance of the specially developed Λ_{CC}, and the construction of the (Λ_{TRD} – Λ_{CC}) template, emphasis was placed on verifying the agreement in the tracker and TRD. The tracker rigidity resolution is studied using the 400 GV test beam data. Performance of the TRD and Λ_{TRD} are verified using using data, and when available, information from ECAL. Agreement between data and simulation are at the percent level.

3.5 Computing fluxes and flux ratios

Overall, template fitting for all 57 rigidity bins gives a total of 3.49×10^5 $\bar{\mathrm{p}}$ events recorded by AMS over four years. The isotropic $\bar{\mathrm{p}}$ flux for the absolute rigidity bin R_i of width ΔR_i is given by

$$\Phi_i^{\bar{p}} = \frac{N_i^{\bar{p}}}{A_i^{\bar{p}} T_i \Delta R_i} \tag{3.1}$$

where the rigidity is defined at the top of AMS, $N_i^{\bar{p}}$ is the number of $\bar{\mathrm{p}}$ in the rigidity bin i, $A_i^{\bar{p}}$ is the corresponding effective acceptance, and T_i is the exposure time.

The template fitting technique has produced a measurement of $N_i^{\bar{p}}$, next $A_i^{\bar{p}}$ and T_i are addressed. Finally, a correction to $N_i^{\bar{p}}$ with the rigidity resolution function to obtain the final flux result is performed.

3.5.1 Effective acceptance

The flux is a measure of rate per unit area (spatial and angular). The area that AMS observes is called the geometric acceptance [104]. Here $A_i^{\bar{p}}$ also includes trig-

ger efficiency, reconstruction efficiency, and selection efficiency. This is the effective acceptance.

The effective acceptance is calculated from the Monte Carlo simulation. The simulation generates particles from a plane with total area $A_{\rm MC}$ (m^2 sr). For each rigidity bin $N_i^{\rm MC}$ particles with an isotropic distribution and power law scaled flux are generated. The number of events that are finally selected after the simulated trigger, reconstruction, and sample selection is $N_i^{\rm select}$. The effective acceptance is then simply $A_i^{\bar{p}} = A_{\rm MC} \times (N_i^{\rm select}/N_i^{\rm MC})$.

The effective acceptance calculation is verified by calculating the geometric acceptance [104], trigger efficiency, reconstruction efficiency, and selection efficiency individually. The geometric acceptance varies from 0.02 to 0.54 m^{2}sr for the most and least restrictive geometries respectively. The trigger efficiency is calculated as the ratio between the physics trigger rate and the rescaled unbiased trigger. Reconstruction and selection efficiencies are calculated by comparing the number of events passing progressively tighter requirements.

3.5.2 Exposure time

Exposure time, T_i, is the active physics data taking time AMS has achieved over the four years used for this analysis. It is calculated in four parts. First, the total data taking time is taken as the sum of the times for all the physics runs included in this analysis. Recall that times when the detector had parts of the ISS in field of view or off-nominal conditions like gas injections have been excluded. Second, times when AMS is in the SAA are subtracted. Third, times when AMS is at low latitude are subtracted depending on the rigidity of each bin. In each bin only times when the particles with those rigidities that would have been excluded from the geomagnetic cutoff selection are subtracted. Above 30 GV there is no reduction in exposure time from the geomagnetic field. Fourth, the observation time is multiplied by the detector live time for each active second. This accounts for the 600 μs digitization dead time after each trigger. The final exposure time over four years totals $\sim 10^8$ seconds.

3.5.3 The effective number of antiprotons and rigidity unfolding

From the raw number of $\bar{\mathrm{p}}$ events calculated from the template fitting normalizations, the correct number of events must be assigned to each rigidity bin in the $\bar{\mathrm{p}}$ flux. Detector resolution effects cause migration in the number of events $N_i^{\bar{p}}$ from rigidity bin R_i to the measured rigidity bins $\tilde{R}_j$ resulting in the observed number of events $\tilde{N}_j^{\bar{p}}$. To correct for this event migration, two unfolding procedures [105, 106] are used to correct the number of observed events.

The first procedure [105] is the one used in the final results. The unfolded flux is obtained iteratively. The flux is initially taken as described by Equation (3.1), without corrections for the rigidity resolution function. On each subsequent iteration, the folded acceptance $\tilde{A}_i^{\bar{p}}$ is calculated for each bin according to

$$\tilde{A}_i^{\bar{p}} = \frac{1}{\Phi_i^{\bar{p}}} \sum_j \Phi_j^{\bar{p}} A_j^{\bar{p}} M_{ij}^{\bar{p}} \tag{3.2}$$

where $M_{ij}^{\bar{p}}$ is the matrix describing the migration probability from bin j to bin i. The weights for the matrix $M_{ij}^{\bar{p}}$ are obtained from the rigidity resolution function as calculated from Monte Carlo simulation.

Next, $\tilde{A}_i^{\bar{p}}$ is parametrized using a spline function. Finally, the number of events in each bin is corrected by a factor of $A_i^{\bar{p}}/\tilde{A}_i^{\bar{p}}$ and the flux is reevaluated using Equation 3.2. Iteration continues until the fluxes between two successive steps agree within 0.1%.

The second procedure [106] is based on a forward unfolding technique. Spline functions are used to parametrize $\tilde{N}_j^{\bar{p}}$. Varying node positions are used to to produce a set of splines. The spline functions are folded with $M_{ij}^{\bar{p}}$ and fit to $\Phi_i^{\bar{p}}$. The average of those spline functions compatible with the observed $\Phi_i^{\bar{p}}$ is used to obtain the final $\tilde{N}_j^{\bar{p}}$.

These two procedures are performed and the results are checked against each other. The difference between the two procedures is $< 0.5\%$. This 0.5% is taken as

the systematic error due to unfolding.

The same procedures are used to compute the flux from the the observed number of 2.42×10^9 p events.

3.5.4 The flux ratio

In addition to the individual corrected fluxes of $\bar{\mathrm{p}}$ and p the ($\bar{\mathrm{p}}$/p) flux ratio is computed. It is defined for each absolute rigidity bin by

$$\left(\frac{\bar{\mathrm{p}}}{\mathrm{p}}\right)_i \equiv \frac{\Phi_i^{\bar{p}}}{\Phi_i^{p}} = \frac{\tilde{N}^{\bar{p}}}{\tilde{N}^{p}} \frac{\tilde{A}_i^{p}}{\tilde{A}_i^{\bar{p}}} \tag{3.3}$$

The exposure time and associated errors cancel; additionally, many systematic effects on $\bar{\mathrm{p}}$/p ratio cancel compared to the individual fluxes.

Chapter 4

Systematic errors

With 3.49×10^5 $\bar{\mathrm{p}}$ events, the detailed study of systematic errors of the $\bar{\mathrm{p}}$ flux and ($\bar{\mathrm{p}}$/p) flux ratio become the most important part of understanding the analysis as over most of the rigidity range they dominate over statistical errors.

There are four sources of systematic errors on the $\bar{\mathrm{p}}$ flux and ($\bar{\mathrm{p}}$/p) flux ratio. The first source affects mostly $\tilde{N}_i^{\bar{p}}$ and, to a much lesser extent, $\tilde{N}_i^{p}$. It includes uncertainties in the definition of the geomagnetic cutoff factor, in the event selection, and in the shape of the templates. The second source affects $\tilde{A}_i^{\bar{p}}$ and $\tilde{A}_i^{p}$. It includes uncertainties in the inelastic cross sections of p and $\bar{\mathrm{p}}$ in the detector materials and in the migration matrices $M_{ij}^{\bar{p}}$ and M_{ij}^{p}. The third source is the uncertainty in the absolute rigidity scale. The fourth source, relevant only for the $\bar{\mathrm{p}}$ flux, is the uncertainty in the normalization of the effective folded acceptance $\tilde{A}_i^{\bar{p}}$. Contributions of these four sources to the systematic errors on the $\bar{\mathrm{p}}$ flux and ($\bar{\mathrm{p}}$/p) flux ratio are discussed below. They are added quadratically to calculate the overall systematic errors.

4.1 Selection stability

The first source of systematic error on $\tilde{N}_i^{\bar{p}}$ and $\tilde{N}_i^{p}$ originate from our original selection of the negative and positive rigidity samples respectively.

To evaluate systematic uncertainties related to the the initial sample selection, the analysis is repeated in each rigidity bin 1000 times with different sets of cut values.

The cut values are varied within 20% of their nominal value with resulting variation in selection efficiency changing up to 10%. This approach is based on the procedure used to verify the selection efficiency in Reference [21].

This uncertainty in $\tilde{N}_i^{\bar{p}}$ amounts to 4% at 1 GV, 0.5% at 10 GV, and rises to 6% at 450 GV. The uncertainty in $\tilde{N}_i^{p}$ is negligible over the entire rigidity range. The effect of varying the selection on the ($\bar{\text{p}}$/p) flux ratio is shown in Figure 4-1.

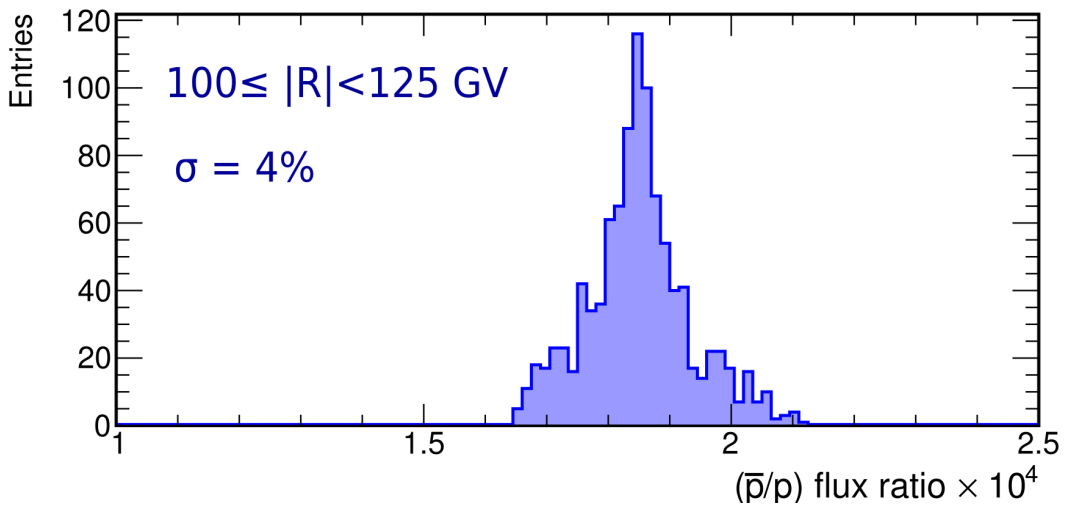

Figure 4-1: The effects of variations in the parameters used to select the positive and negative rigidity samples. The parameters are randomly selected within 20% variation of their nominal values to produce up to 10% variation of selection efficiency. This results in a net 4% RMS on the ($\bar{\text{p}}$/p) flux ratio for the $100 \leq |R| < 125$ GV bin.

4.1.1 Geomagnetic cutoff and solar modulation

At the lowest rigidities, the selection that most affects this analysis is the selection for primary particles. This is well controlled by a good understanding of geomagnetic effects. The Earth's magnetic field has been extensively measured and varies from 23 μT to 65 μT at the Earth's surface. Additionally, satellite measurements provide magnetic field measurements at a variety of altitudes. This allows for the tuning of a multipole model of the geomagnetic field known as the International Geomagnetic Reference Field [96, 97]. This detailed model accounts for secular variation and is continually updated.

As mentioned in Section 3.1 only primary cosmic rays are selected. This is done by requiring the reconstructed track rigidity to exceed the maximum geomagnetic cutoff by a factor of 1.2. The geomagnetic cutoff is defined as the rigidity below which no primary galactic cosmic ray can penetrate the geomagnetic field to reach AMS. This is calculated using backtracing as shown schematically in Figure 4-2.

Systematic errors from this cutoff factor are calculated by varying the geomagnetic cutoff factor from 1.2 to 1.4. The resultant variation in selection efficiency is taken as the systematic uncertainty which is ∼1% at 1 GV and negligible above 2 GV for both $\tilde{N}_i^{\bar{p}}$ and $\tilde{N}_i^{p}$.

Finally, the effects of calculating the cutoff by backtracing the IGRF model [97] are checked by making an alternative selection using a dipole approximation Størmer cutoff [107]. The selection with the IGRF and Størmer cutoffs agree within the stated systematic uncertainty.

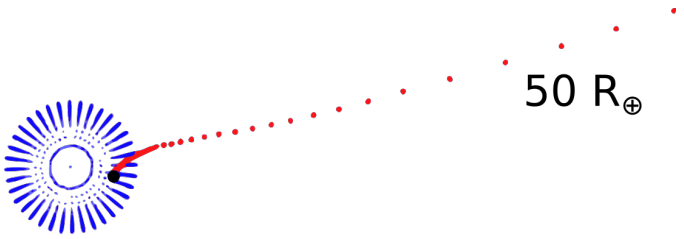

Figure 4-2: A schematic of the backtracing algorithm used to compute the geomagnetic cutoff. The cutoff is calculated by numerically integrating the particle trajectory through the most recent IGRF geomagnetic model [97]. This procedure is referred to as backtracing. The integration is done to 50 Earth radii, $R_\oplus$. The cutoff is calculated for both the positive and negative particle hypothesis. Effects from the geomagnetic cutoff only affect particles below 30 GV and are less pronounced during the parts of the ISS orbit near the equator.

4.2 Template shape

The second source of error on $\tilde{N}_i^{\bar{p}}$ originates from the template fitting procedure.

While the template fitting produces a well described statistical error, there remains the possibility of some systematic error introduced by the template shapes used. Systematic uncertainty in the shape of the fit template are found to affect only $\tilde{N}_i^{p}$.

It becomes particularly important at rigidities above 150 GV where charge confusion p enter the $\bar{p}$ sample.

Recall that three template shapes are used for the fit in the high absolute rigidities sample—the $\bar{p}$ signal template, the e^- background template, and the charge confusion p template.

The $\bar{p}$ signal template is defined by the p sample reconstructed with correct charge-sign. The validity of this method was checked with the AMS Monte Carlo simulation and for the high-resolution low-rigidity data. This means the template for correct charge sign is extracted from a high-statistics unbiased data sample, therefore the systematic effects are negligible.

The e^- template from the Monte Carlo simulation is validated with a high-purity high-statistics e^- data sample selected with Λ_{ECAL}. This does not contribute significantly to the systematic error.

The systematic error due to the uncertainty in the shape of the charge confusion p template originates from the uncertainties of the p flux in the TV region and from the uncertainties of the p rigidity resolution function. The former is estimated by varying the spectral index of the p flux within the accuracy of the AMS p flux measurement [25]. The latter is estimated by comparing the charge confusion amount predicted by the Monte Carlo simulation with the one obtained from the fit of the three template shapes to the negative rigidity data. Overall, the systematic error from the templates is estimated to be <1% below 30 GV, increasing to 12% at 450 GV.

4.2.1 Charge confusion template

Since the charge confusion p template is the only template that contributes significantly to the systematic error on $\tilde{N}_i^p$ an additional study of charge confusion p is discussed here.

Again, charge confusion p are p which are reconstructed in the tracker with negative rigidity due to the finite tracker resolution or due to interactions with the detector materials. A detailed accounting of these charge confusion p is made using the AMS Monte Carlo simulation (Section 3.4), Λ_{CC}, and template fitting. There is, however,

also a data driven estimate for the amount of charge confusion p. This ensures that the shape of the charge confusion p background templates from the Monte Carlo simulation does not introduce bias into the $\bar{p}$ identification.

This data driven analysis is performed as a completely independent analysis covering $|R| > 30$. The analysis is based on the linear regression method [99, 108] and covers the acceptance which includes L1, L9, and ECAL.

In this data driven method, a weighted sum is constructed from a set of measured quantities sensitive to the finite tracker resolution and interactions with the detector materials. This set includes information from the TRD, TOF, tracker, ACC, and ECAL. In particular, the tracker information includes the χ^2/d.o.f., the rigidity reconstructed using different combinations of tracker layers, and the maximum distance of the tracker hits from the fitted track. The weights of individual quantities are optimized to maximize the separation between the $\bar{p}$ signal and the charge confusion p background. The resultant sums are nearly Gaussian for both the $\bar{p}$ signal and the charge confusion p background. This near-Gaussian behavior is a result of a generalization of the central limit theorem.

These sums are taken as templates (i.e., a Gaussian distribution with $\sim 1\%$ non-Gaussian tails) that do not rely on the Monte Carlo simulation. The non-Gaussian tails are evaluated using iterative fits.

The results of this data driven analysis agree within the systematic errors estimated for the full Monte Carlo simulation-based template fitting.

As a final check, the performance of Λ_{CC} is compared in performance to the similarly designed classifier for $e^{\pm}$ data. For the e^+ flux measurement the expected charge confusion comparisons are made between expectations from Monte Carlo simulation and the measured e^- flux [23], the observed charge confusion from fitting, and the estimated charge confusion from E/p matching between the tracker and the ECAL. These agree within the stated systematic errors assigned to the charge confusion template fit.

4.3 Absolute rigidity scale

The third source of systematic errors on $\tilde{N}_i^{\bar{p}}$ and $\tilde{N}_i^{p}$ originate from the systematic uncertainty on the absolute rigidity scale of the measurement.

There are two contributions to the systematic uncertainty on the rigidity scale. The first is due to residual tracker misalignment. From the 400 GV p test beam data, residual tracker misalignment is measured to be less then 1/300 TV^{-1}. The agreement in absolute rigidity measurement and rigidity resolution function for test beam data is shown in Figure 4-3. The residual tracker misalignment is estimated directly from ISS flight data for $\mathrm{e}^{\pm}$ in Reference [25]. It is found to be 1/26 TV^{-1} for $\mathrm{e}^{\pm}$ and is limited by the low rate of high energy e^{+} events. The second systematic error on the rigidity scale arises from uncertainties of $\sim$0.25% in the magnetic field map for the AMS inner tracker, and 0.1% uncertainties in the temperature correction to the magnetic field map.

These absolute rigidity scale uncertainties are weighted by the rigidity dependence of the observed fluxs. Together these sources of error are negligible below 10 GV and gradually increase to $\sim$1% at 450 GV for the $\bar{\mathrm{p}}$ and p fluxes. These errors on absolute rigidity scale have compounding effects on the measured p and $\bar{\mathrm{p}}$ fluxes, therefore the error on the ($\bar{\mathrm{p}}$/p) flux ratio gradually increases to $\sim$2% at 450 GV.

4.4 Antiproton and proton cross section uncertainties

The primary source of systematic errors on the effective acceptances $\tilde{A}_i^{\bar{p}}$ and $\tilde{A}_i^{p}$ arise from the efficiency factors included in the effective acceptance definition as well as effects from the unfolding. The AMS geometry is described at high fidelity as shown in Figure 2-1. The trigger and reconstruction efficiencies, however, depend on interaction cross sections. The migration matrices $M_{ij}^{\bar{p}}$ and M_{ij}^{p} used to compute $\tilde{A}_i^{\bar{p}}$ and $\tilde{A}_i^{p}$ from $A_i^{\bar{p}}$ and A_i^{p} respectively also depend on interaction cross sections since the probability of elastic and inelastic scattering affect the rigidity resolution function.

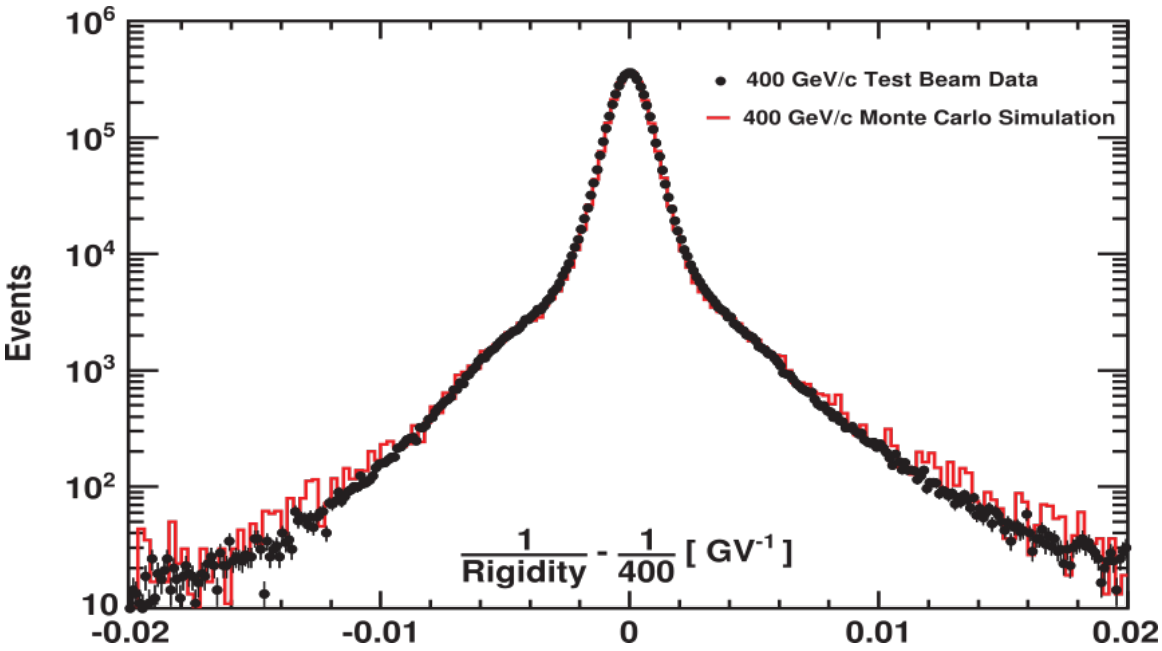

Figure 4-3: A comparison between the 400 GV p test beam taken at the CERN SPS and the AMS Monte Carlo simulation. The data show agreement of the absolute rigidity scale to the level of 1/300 TV^{-1}. The simulation reproduces the Gaussian core and non-Gaussian tails of the rigidity resolution function. This good matching allows for an accurate description of charge confusion and bin-to-bin migration.

Since the spectrometer is mostly made of carbon and aluminum, the cross sections for p + C and p + Al dominate the $\tilde{A}_i^p$ uncertainties. The measurements of these cross sections vary within 10% at 1 GV and 4% at 300 GV [109, 110, 110–113]. The cross section measurements and model for p + C are shown in Figure 4-4. Similarly the cross section measurements for $\bar{\text{p}}$ are mostly older and vary within 10% [114–117]. The cross section measurements and model for $\bar{\text{p}}$ + C are shown in Figure 4-5. The band in the figures represents the range through which the model parameters are varied to compute the systematic error from these cross section uncertainties.

The corresponding systematic error on $\tilde{A}^{\bar{p}}$ is found to be 4% at 1 GV and ∼1% above 50 GV. The error on $\tilde{A}^p$ is found to be 2.5% at 1 GV and ∼1% above 50 GV. These values are larger than those in Reference [25] due to the varying acceptance used in this analysis.

The systematic errors on $\tilde{A}_i^{\bar{p}}$ and $\tilde{A}_i^p$ due to the cross section uncertainties are independent, therefore they are added in quadrature to estimate the systematic error

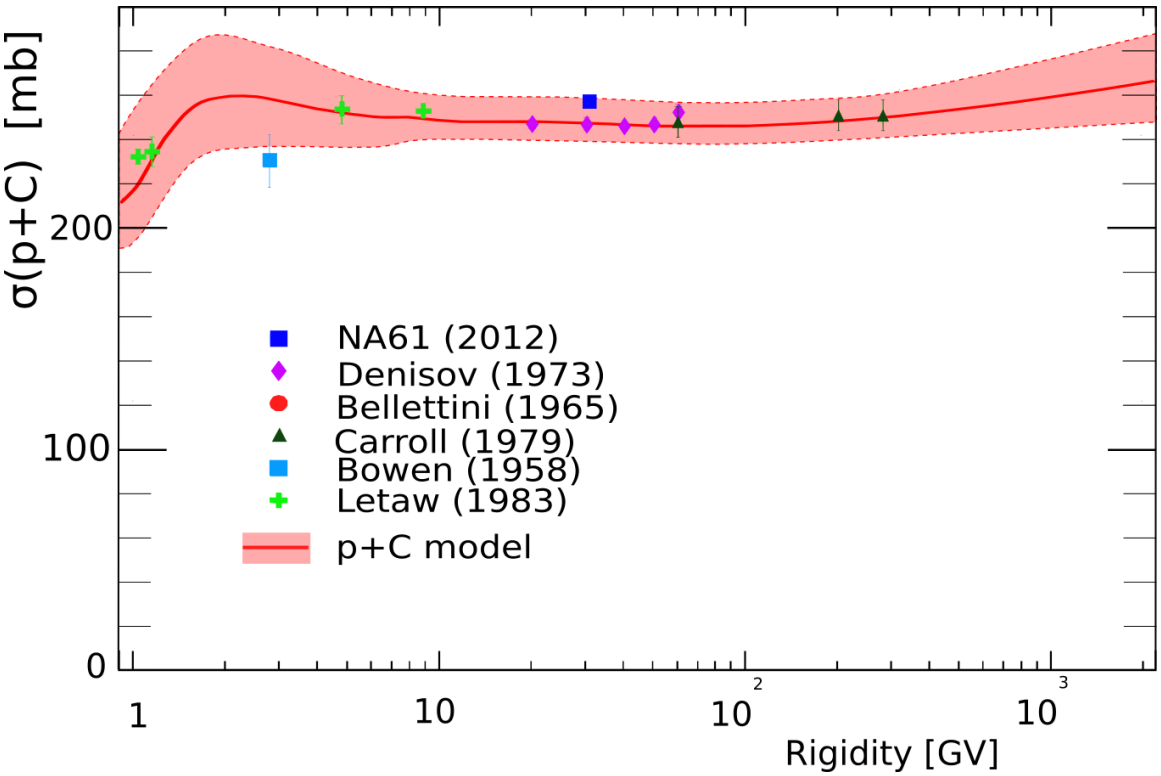

Figure 4-4: The cross section measurements for p + C [109, 110, 110–113]. The model and its variation in the AMS Monte Carlo simulation is overlaid. The variation accounts for the cross section uncertainties and are propagated to the final result.

on the $\tilde{A}^{\bar{p}}/\tilde{A}^{p}$ ratio. This effect is shown in Figure 4-6.

The systematic uncertainty in the migration matrix M^{p}_{ij} is studied by comparing the test beam data at 400 GV with the Monte Carlo simulation as shown in Figure 4-3. The rigidity resolution function $\Delta(1/R)$ has a pronounced Gaussian core of width σ and non-Gaussian tails spanning beyond 2.5σ from the center [25]. Uncertainties in the core and in the tails of the $\bar{\text{p}}$ migration matrix $M^{\bar{p}}_{ij}$ are assumed to be the same as for M^{p}_{ij}. Varying both the width of the core and the amount of non-Gaussian tails is done in the same way as in Reference [25]. This yields a systematic error of 1% below 200 GV and 1.5% at 450 GV for both $\tilde{A}^{\bar{p}}$ and $\tilde{A}^{p}$. These systematic errors partially cancel in the $\tilde{A}^{\bar{p}}/\tilde{A}^{p}$ ratio, yielding uncertainties of 1% at 1 GV and $<$0.5% above 2 GV. Note that the $\tilde{A}^{\bar{p}}/\tilde{A}^{p}$ ratio decreases from 1.15 at 1 GV to 1.04 at 450 GV due to the varying difference of interaction cross sections for p and $\bar{\text{p}}$, and due to bin-to-bin event migration.

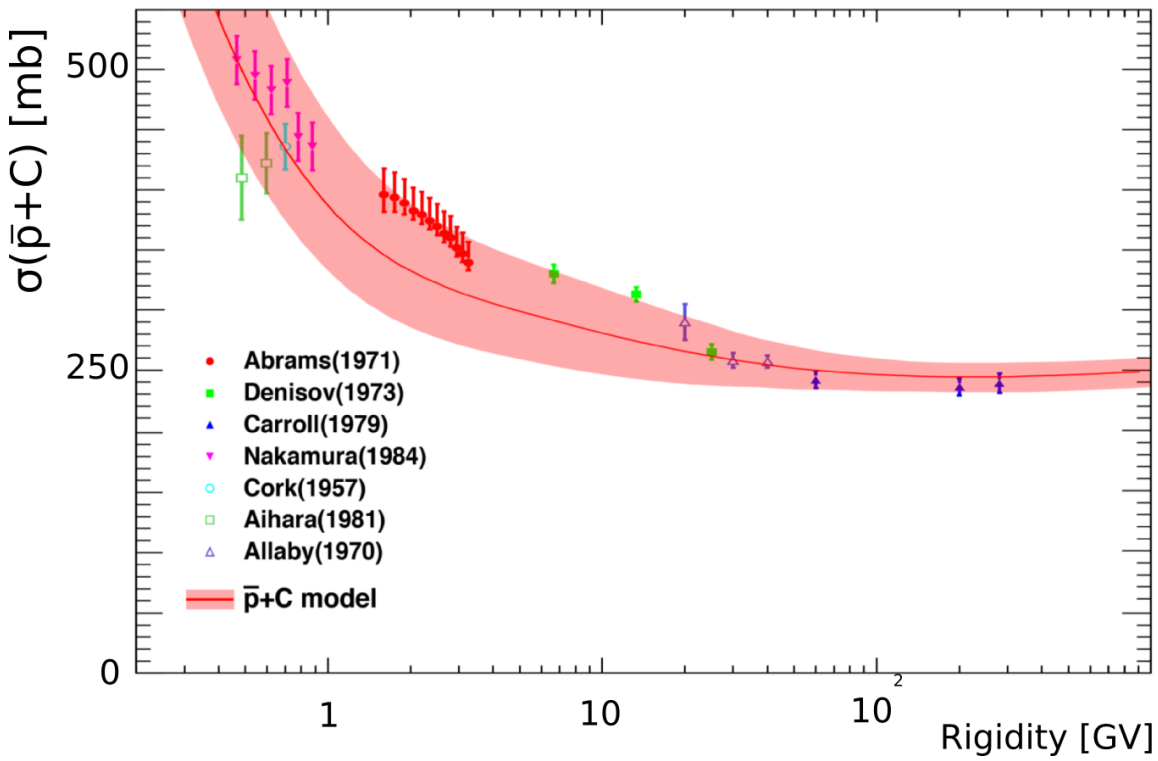

Figure 4-5: The cross section measurements for $\bar{p}$ + C [114–117]. The model and its variation in the AMS Monte Carlo simulation is overlaid.

4.5 Summary of errors

A complete description of the analysis used to arrive at the p flux, $\bar{p}$ flux, and ($\bar{p}$/p) flux ratio as well as the evaluation of the associated errors has been presented. The detailed listing of these values as a function of the absolute rigidity at the top of the AMS detector along with the number of observed $\bar{p}$ events $\tilde{N}^{\bar{p}}$ are available in Appendix A. A summary of the errors is shown in Figure 4-7.

The statistical and systematic error contributions to the total error in the flux and flux ratio vary with rigidity. For $1.00 \leq |R| < 1.33$ GV the statistical error dominates, for $1.33 \leq |R| < 1.71$ GV the errors are comparable, for $1.71 \leq |R| < 48.5$ GV the systematic error dominates, for $48.5 \leq |R| < 108$ GV the errors are comparable, and for $108 \leq |R| < 450$ GV statistical error dominates. This means that with continued data taking, AMS can continue to improve this result over a broad rigidity range.

As a final and important check, several other independent analyses were performed

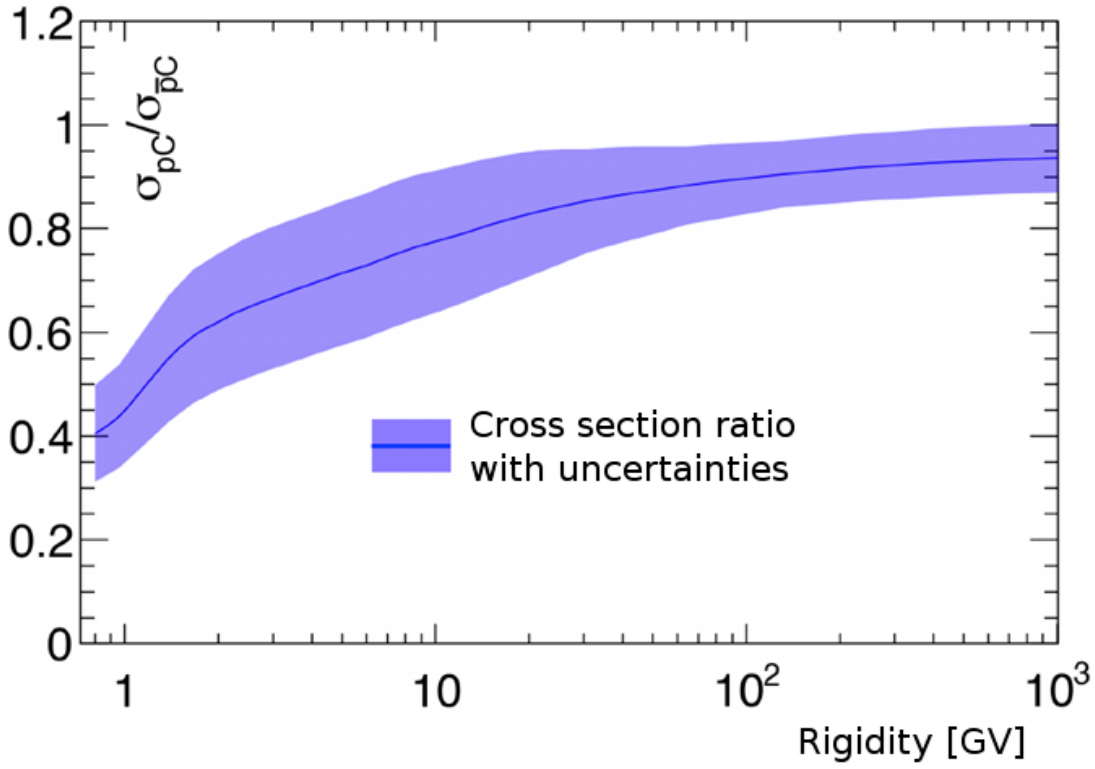

Figure 4-6: A comparison of cross section ratio uncertainties. The cross section uncertainties for $\bar{p}$ + C and p + C are independent so they must be combined in the computation of the $\bar{p}$/p flux ratio uncertainties.

on the same data sample by different study groups. The results of those analyses are consistent within systematic errors with the analysis in this thesis.

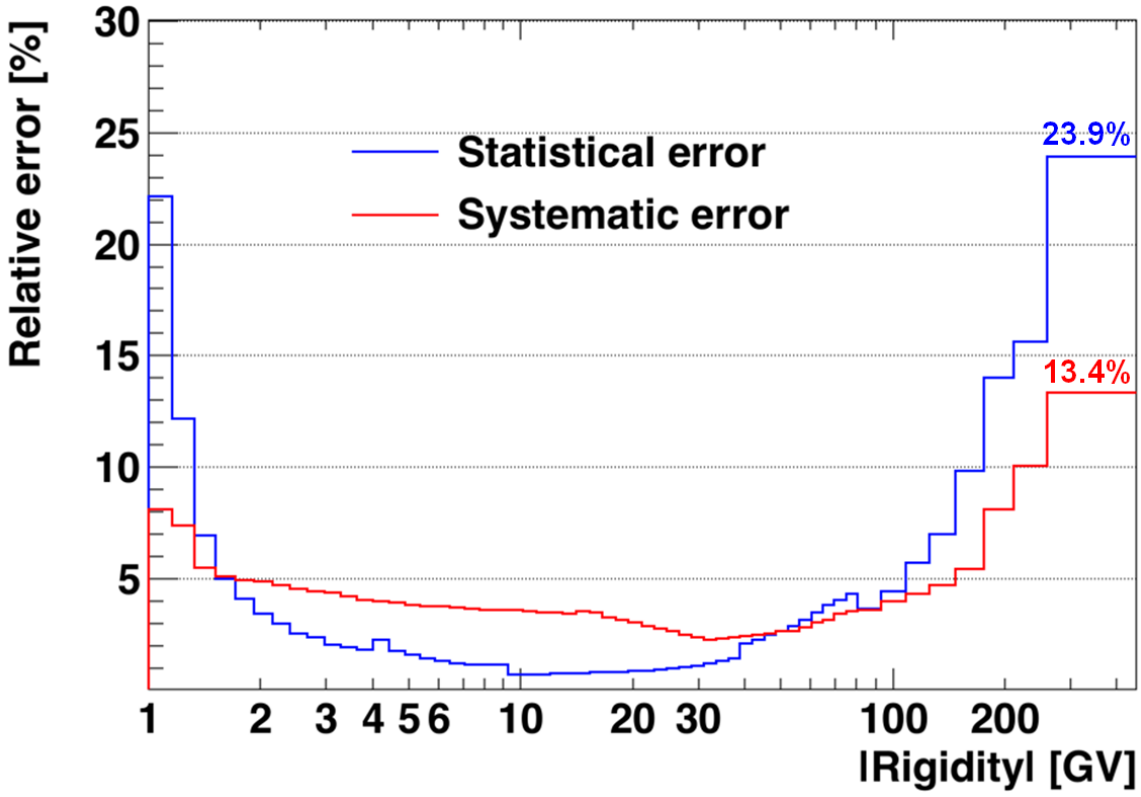

Figure 4-7: A summary of the errors on the $\bar{p}/p$ flux ratio. At low and high rigidities the statistical error dominates. At intermediate rigidities the systematic error dominates. Statistical errors will be reduced with continued AMS data taking. Systematic error will be reduced with future terrestrial measurements reducing the uncertainty on the cross section for $\bar{p}$ and p interacting with AMS materials and continued improvement in the understanding of the AMS detector.

Chapter 5

Results

AMS has now measured the fluxes of e^+ and e^- [23] and the flux of p [25]. These measurements are made with the same detector over the period spanning 19 May 2011 – 26 November 2013. The analysis presented in this thesis has met the unique challenges of measuring $\bar{p}$ with AMS. The $\bar{p}$ flux, p flux, and $\bar{p}/p$ flux ratios measured with this analysis include an additional year and a half, 19 May 2011 – 26 May 2015.

There are time dependent solar effects on these fluxes that AMS has observed in these intervals. The detailed measurement of the time dependent solar modulation of primary cosmic rays fluxes with AMS on the ISS will be published at a later date. In particular the $\bar{p}$ flux has never been reported over a full solar cycle. AMS will be able to make this measurement, despite the geomagnetic cutoff, due to its large acceptance and the stability of both AMS and the ISS.

Within the accuracy of the analysis presented here and in Reference [23, 25], the time dependent solar effects are observable for $\bar{p}$, e^+, and e^- with $|R| < 20$ GV and for p with $|R| < 10$ GV.

For the study of the rigidity dependence of the flux ratios of elementary particles, $|R| > 10$ GV is chosen as this is where the time dependent solar effects for p are small and the uncertainties are dominated by the accuracies of the measurements of e^+, e^-, and $\bar{p}$. This enables the study of the overall rigidity dependent behavior of different fluxes without significant solar effects.

5.1 The antiproton-to-proton flux ratio

The first result presented is the ($\bar{p}$/p) flux ratio. The flux ratio is complementary to the positron fraction measurement [21, 22] and has reduced errors compared to the individual fluxes.

Figure 5-1 shows the measured ($\bar{p}$/p) flux ratio. It is compared with the two earlier experiments from this century [56, 63]. For GV rigidities, AMS doubles the extent of the rigidities measured and increases the precision and accuracy throughout.

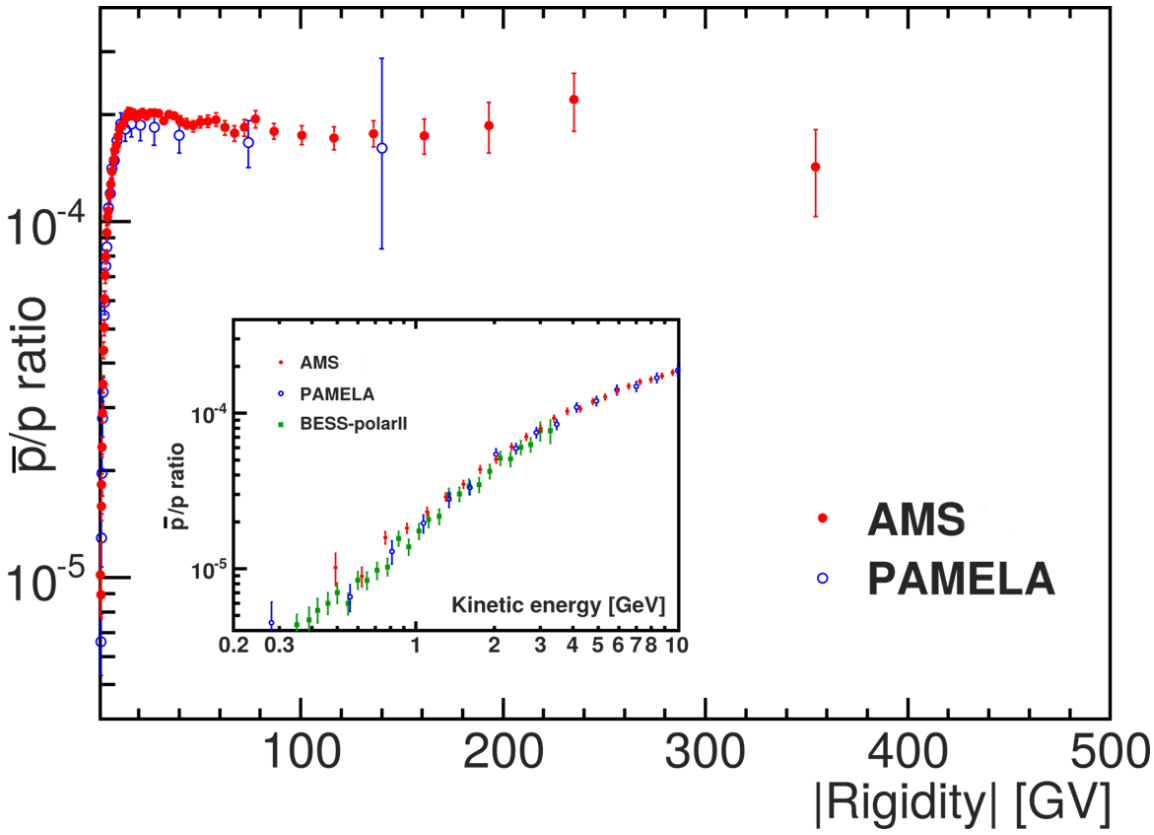

Figure 5-1: A precision measurement of the ($\bar{p}$/p) flux ratio by AMS. The flux ratio is measured for primary cosmic rays in the absolute rigidity range from 1 to 450 GV. The errors combine the systematic errors as well as the statistical errors based on 3.49×10^5 $\bar{p}$ events and 2.42×10^9 p events. Also shown are previous experiments [56, 63] who report their results in kinetic energy. Before this measurement by AMS only four events above 100 GV had been observed.

To minimize the systematic error for the flux ratio, the 2.42×10^9 p selected with the same acceptance, time period, and absolute rigidity range as the $\bar{p}$ are used, rather than the flux as presented in Reference [25]. From 10 to 450 GV, the values of the p

flux are identical to 1% of those quoted in [25].

As seen from Figure 5-1, above ∼60 GV the ratio appears to be rigidity independent. This is the first time this flatness has been apparent, and is inconsistent with the predictions made by pre-AMS models [68].

5.2 Unexpected flatness

Since the flat behavior of the ($\bar{\mathrm{p}}$/p) flux ratio is unexpected, the flatness is quantified in three ways. First, the region which the flatness is apparent is defined. Second, it is determined if a flat flux ratio is a sufficient description. Third, the spectral index is calculated, which is a useful overall characterization for cosmic ray fluxes.

5.2.1 Sliding window fit

To estimate the lowest rigidity above which the ($\bar{\mathrm{p}}$/p) flux ratio is rigidity independent, rigidity intervals with starting rigidities from 10 GV and increasing bin by bin are used. The ending rigidity for all intervals is fixed at 450 GV.

Each interval is split into two sections with a boundary between the starting rigidity and 450 GV. Each of the two sections is fit with a constant and two mean values of the ($\bar{\mathrm{p}}$/p) flux ratio are obtained. The lowest starting energy of the interval for which the two sections give consistent mean values at the 90% C.L. for all boundaries defines the lowest limit. This procedure is illustrated in Figure 5-2.

This sliding window fit yields 60.3 GV as the lowest rigidity above which the ($\bar{\mathrm{p}}$/p) flux ratio is rigidity independent.

5.2.2 Minimal fit

To further probe the behavior of the flux ratio the best straight line fit over a rigidity interval is defined as

$$(\bar{p}/p) = C + k \times (|R| - R_0), \tag{5.1}$$

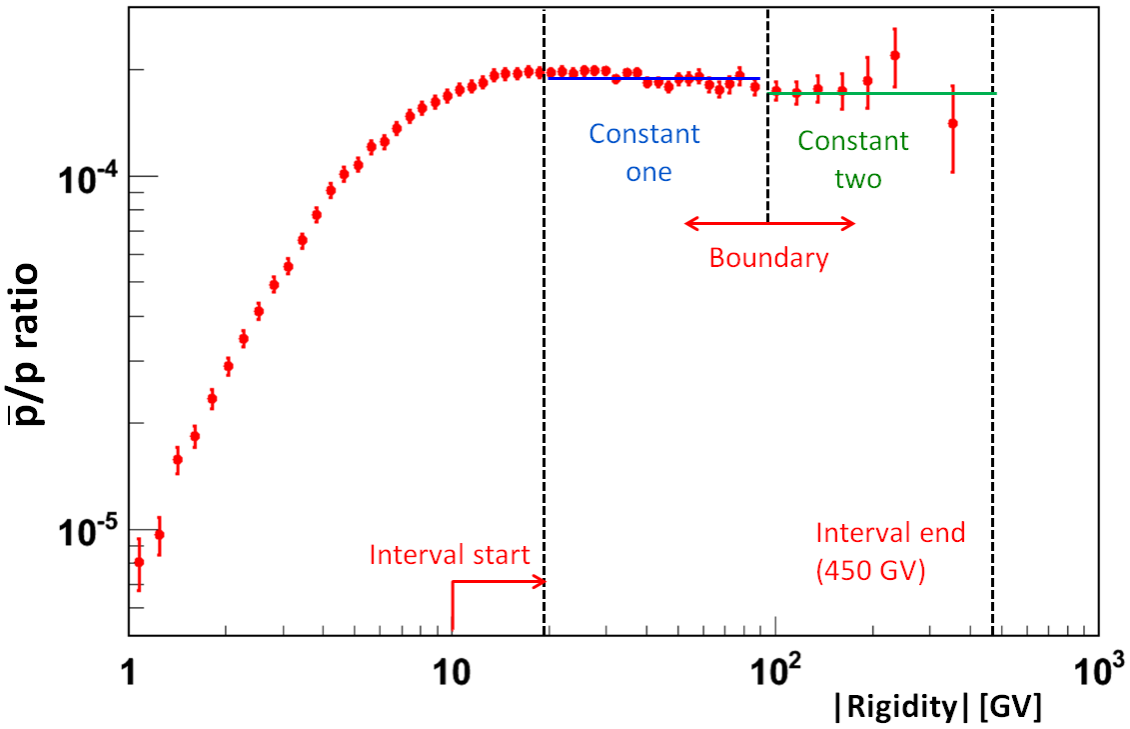

Figure 5-2: A schematic of the sliding window fit used to determine the range where the $(\bar{p}/p)$ flux ratio is effectively rigidity independent. A moving starting point is used to define the interval under examination. The interval is split by a boundary and mean values are calculated by fitting a constant. When the means are consistent at the 90% C.L. for all boundaries within the interval, the interval is said to be consistent with a flat $(\bar{p}/p)$ flux ratio. It is determined with this procedure that above 60.3 GV the $(\bar{p}/p)$ flux ratio is effectively flat.

where C is the value of the flux ratio at R_0, k is the slope, and R_0 is the the mean value of $|R|$ over the interval weighted with the statistical and uncorrelated systematic errors. This is chosen to minimize the correlation between the fitted values of C and k.

To begin with, the fit with Equation (5.1) is performed for the whole rigidity region above 60.3 GV. The selection of 60.3 GV was determined in Section 5.2.1. For this range, $R_0 = 91$ GV. The fitted value of the slope at 68% C.L. is $k = (0.7 \pm 0.9) \times 10^{-7}$ GV^{-1}. This is consistent with zero, meaning a constant would be sufficient to describe the $(\bar{p}/p)$ flux ratio.

A fit of Equation (5.1) to the data over a sliding window of rigidity ranges is also performed. For the $(\bar{p}/p)$ flux ratio, the width of the window varies with rigidity to

have sufficient sensitivity to the slope k such that each window covers between four and eight bins of the flux ratio result shown in Figure 5-1. The variations of C and slope k for the ($\bar{\text{p}}$/p) flux ratio are shown in Figure 5-3. At low rigidity, the slope k crosses zero. From this it is clear that the ratio reaches a maximum at $\sim$ 20 GV. This is also seen in the parameter C.

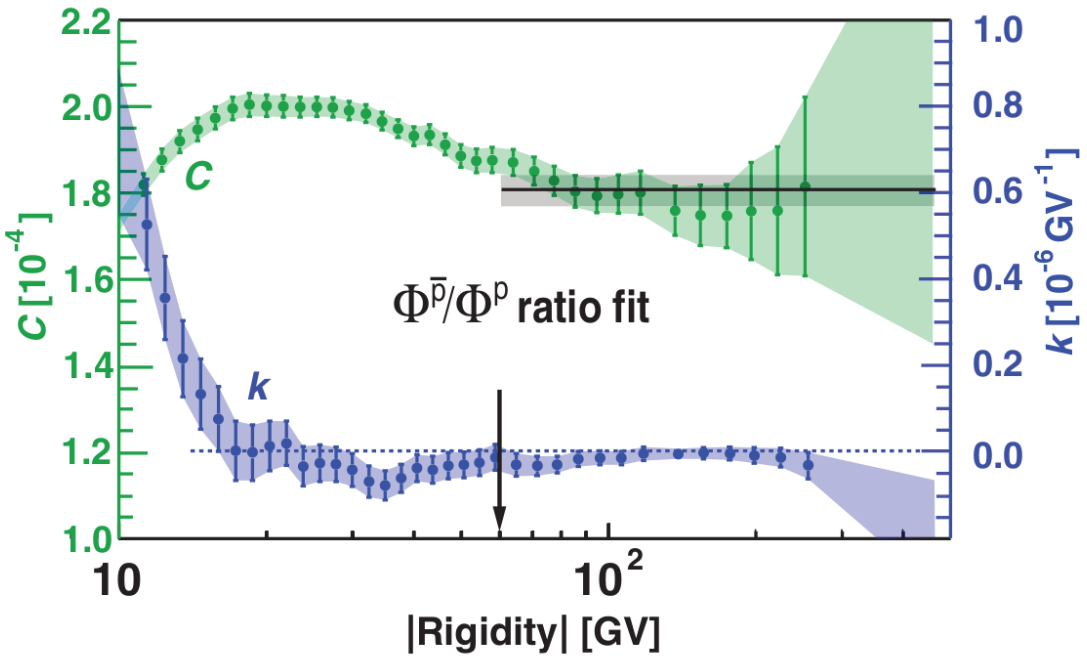

Figure 5-3: The results of linear fits over a sliding window. A fit to the ($\bar{\text{p}}$/p) flux ratio is performed over a sliding rigidity window using Equation (5.1). The parameter C of the fit is shown on the left axis and the parameter corresponding to slope k is shown on the right axis. The shaded regions indicate the errors that are correlated between adjacent points. The points are placed at R_0. The dashed blue line at $k = 0$ is to guide the eye. The black arrow indicates the lowest rigidity above which the flux ratio is consistent with being rigidity independent as determined in Section 5.2.1. The black horizontal band shown above this rigidity gives the mean value and the 68% C.L. error on the absolute magnitude of the flux ratio.

5.2.3 Spectral index

In addition to simple fits to help quantify the shape of ($\bar{\text{p}}$/p) flux ratio, the high density of data points allows a study of the $\bar{\text{p}}$ flux spectral index, $\gamma_{\bar{p}}$. The spectral index is useful because simplistic expectations for cosmic ray fluxes often produce a

power law [7] where the flux, $\Phi^{\bar{p}}$, as a function of rigidity is described by

$$\Phi^{\bar{p}}(R) \propto |R|^{\gamma_{\bar{p}}}. \tag{5.2}$$

The measured $\gamma_{\bar{p}}$ is calculated over independent rigidity intervals, with a variable width, to have sufficient sensitivity. It is calculated from data using the relationship

$$\gamma_{\bar{p}} = \frac{d[\log(\Phi^{\bar{p}})]}{d[\log(|R|)]}. \tag{5.3}$$

The result is shown in Figure 5-4 along with the AMS result on the p spectral index, γ_p [25]. As seen over the four lowest rigidity points, $|R| < 60.3$ GV, $\gamma_{\bar{p}}$ decreases more rapidly than γ_p and for the highest rigidity interval, $60.3 \leq |R| < 450$ GV, $\gamma_{\bar{p}}$ is consistent with γ_p.

5.3 The rigidity dependence of elementary particles in cosmic rays

Now that the new measurement of the ($\bar{\text{p}}$/p) flux ratio has been described, the fluxes and flux ratios of all the elementary particles in cosmic rays are presented. The unexpected flatness above 60.3 GV in the ($\bar{\text{p}}$/p) flux ratio has been shown and is also apparent when the fluxes are plotted together. This is done in Figure 5-5. In this figure the p and $\bar{\text{p}}$ fluxes are plotted on different scales to show the similarity in shape made apparent by the ($\bar{\text{p}}$/p) flux ratio.

The fluxes of e^+ and e^- measured by AMS starting from 19 May 2011 [23] are also shown in Figure 5-5. Remarkably, the e^+ flux has the same shape as the p flux and $\bar{\text{p}}$ flux, but the e^- flux does not.

The points in Figure 5-5 are placed along the abscissa at $\hat{R}$ calculated for a flux $\propto |R|^{-2.7}$ [118]. As mentioned above this study is limited to $|R| > 10$ GV—above most time dependent solar effects.

To quantify the similarity in shape the flux ratios are also studied. This is done

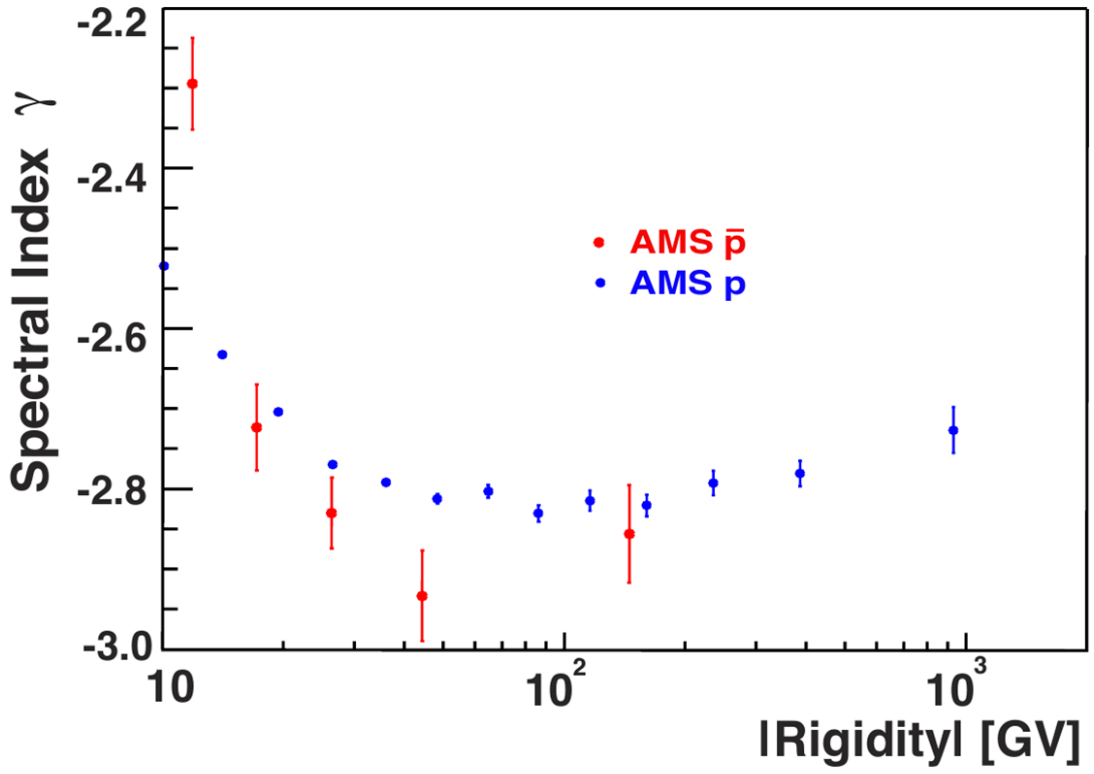

Figure 5-4: The spectral index γ vs $|R|$ of the $\bar{\mathrm{p}}$ flux, where AMS measures for the first time the highest rigidity $\bar{\mathrm{p}}$ point corresponding to $60.3 \leq |R| < 450$ GV, compared with the p flux spectral index [25]. The spectral index for $\bar{\mathrm{p}}$ with $60.3 \leq |R| < 450$ GV is consistent with the p spectral index. The error bars correspond to the quadratic sum of the statistical and uncorrelated systematic errors. Horizontally, the points are placed at the abscissa ($\hat{R}$) calculated for a flux $\propto |R|^{-2.7}$ [118].

in the same way as for the ($\bar{\mathrm{p}}$/p) flux ratio. Using one instrument to do this allows the correlation of the errors to be taken into account. For the $\bar{\mathrm{p}}/\mathrm{e}^+$ flux ratio the rigidity independent interval is $60.3 \leq |R| < 450$ GV. Fitting Equation (5.1) over this interval yields $k(\bar{\mathrm{p}}/\mathrm{e}^+) = (-2.8 \pm 3.2) \times 10^{-4}$ GV^{-1}. For the p/e^+ ratio, the rigidity independent interval is $59.13 \leq |R| < 500$ GV and $k(\mathrm{p}/\mathrm{e}^+) = (-0.9 \pm 1.0)$ GV^{-1}. These fits are shown in the top panel of Figure 5-6 together with the 68% C.L. range of the fit parameters.

In the bottom panel of Figure 5-6 the measured AMS ($\bar{\mathrm{p}}/\mathrm{e}^-$) and ($\mathrm{p}/\mathrm{e}^-$) flux ratios are shown. Both of these flux ratios exhibit rigidity behavior which is distinct from that observed in the ($\bar{\mathrm{p}}$/p), ($\bar{\mathrm{p}}/\mathrm{e}^+$), and ($\mathrm{p}/\mathrm{e}^+$) flux ratios. This rigidity independence

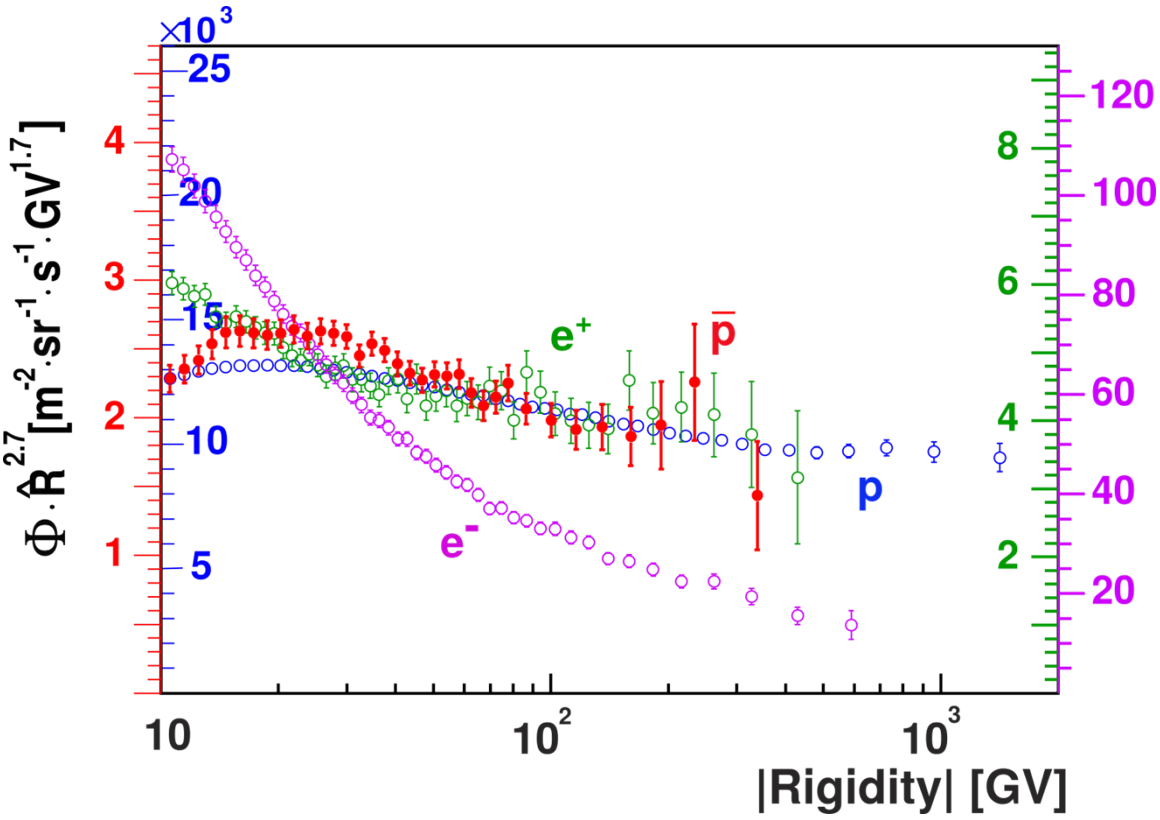

Figure 5-5: The fluxes of all the elementary particle in cosmic rays. AMS has now measured the fluxes for e^-, e^+, $\bar{p}$, and p. The scales for these fluxes are adjusted to show them on the same plot. Note the similar shape for e^+, $\bar{p}$, and p. Note, however, that e^- have a different rigidity behavior.

seen from the best fit slopes to the $(\bar{p}/p)$, $(\bar{p}/e^+)$, and (p/e^+) flux ratios is a new observation.

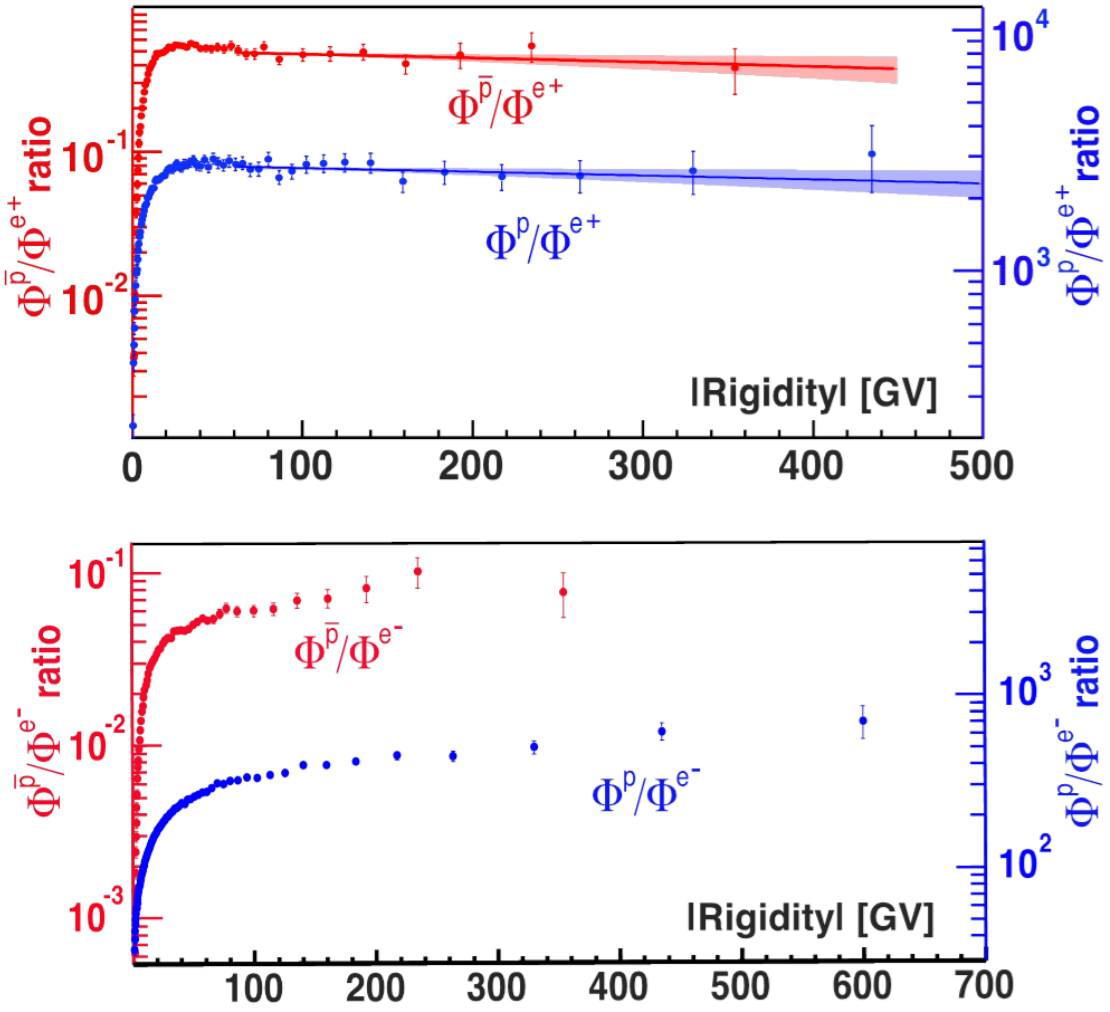

Figure 5-6: The flux ratios of elementary particles in cosmic rays. In the top panel the $(\bar{p}/e^{+})$ and (p/e^{+}) flux ratios are shown. Also shown is the best fit using Equation (5.1) along with the shaded 68% C.L. range of the fit parameters. The flux ratios are consistent with being flat above ∼60 GV. The bottom panel shows the $(\bar{p}/e^{-})$ and (p/e^{-}) flux ratios. These show rigidity dependence.

Chapter 6

Conclusions and outlook

A new measurement of the $\bar{p}$ flux and the $(\bar{p}/p)$ flux ratio made with AMS aboard the ISS has been presented. This measurement has been combined with the simultaneous AMS measurement of the other charged elementary particle cosmic ray fluxes. These fluxes are shown in Figure 5-5. Further more, a study of the the flux ratios has also been presented.

These studies cover the previously unexplored absolute rigidity range from ∼60 to ∼500 GV. The $\bar{p}$, p, and e^+ fluxes are found to have nearly identical rigidity dependence and the e^- flux exhibits a different rigidity dependence. In the absolute rigidity range below 60 GV, the $(\bar{p}/p)$, $(\bar{p}/e^+)$, and (p/e^+) flux ratios each reaches a maximum. These are new observations of the properties of elementary particles in the cosmos.

6.1 Future outlook

The flux measurements made by AMS shown in Figure 5-5, as well as the flux ratio measurements shown in Figures 5-1 and 5-6 and in [21] are the first detailed, percent-level measurements of elementary particles in primary cosmic rays for the GV rigidity range. These measurements are not consistent with pre-AMS predictions [8–11, 68].

Like the positron fraction result in Reference [21], this new observation of the $(\bar{p}/p)$ flux ratio has generated a number of explanations, some of which try to make

a simultaneous fit to all the AMS flux and flux ratio measurements. These include new models for sources like pulsars and supernova remnants *e.g.* Reference [119]. Other explanations include dark matter models. Just four examples of resulting dark matter explanations are provided in References [120–123].

In addition to these exotic interpretations, significant work has been done to improve cosmic ray propagation models by including more sophisticated diffusion process [124] and by reducing the errors associated with cross section uncertainties [41].

6.1.1 The boron-to-carbon flux ratio

One of the largest reductions in uncertainties on the propagation of cosmic rays will come from the measurement of nuclei collected by AMS. The most recent nuclei ratio measurement by AMS is the boron to carbon flux ratio (B/C) [27]. In particular (B/C) constrains diffusion parameters in cosmic ray propagation models. Many corrections to these models to account for the flat $\bar{\mathrm{p}}$/p flux ratio above 60.3 GV and positron fraction excess produce a deviation from a single power law for the (B/C) ratio. The AMS measurements, however, show that above 65 GV, the (B/C) ratio is well described by a single power law. In fact the spectral index, $\gamma_{B/C}$, was measured as $\gamma_{B/C} = 0.333 \pm 0.014$ (fit) $\pm$ 0.005 (syst). This is in good agreement with the Kolmogorov theory of turbulence which predicts the value of $\gamma_{B/C}$ to asymptotically approach 1/3 [125].

This measurement of (B/C) has allowed for new studies on the compatibility of the ($\bar{\mathrm{p}}$/p) flux ratio and positron fraction with the conventional understanding of collisions and propagation of cosmic rays [126].

6.1.2 Continued observations to 2024 and beyond

With its resilient design, AMS is capable of operating throughout the lifetime of the ISS, currently scheduled to operate at least to the year 2024. In that time, AMS will continue to measure nuclei and isotopes up to iron. Additionally the flux of e^+ and

$\bar{p}$ are limited by statistics at highest and lowest rigidity—these measurements will continue to improve with continued data taking. A projection of the ($\bar{p}$/p) flux ratio measurement by AMS in 2024 is shown in Figure 6-1. Finally, novel techniques [127] will allow AMS to extend the reach of these and other measurements.

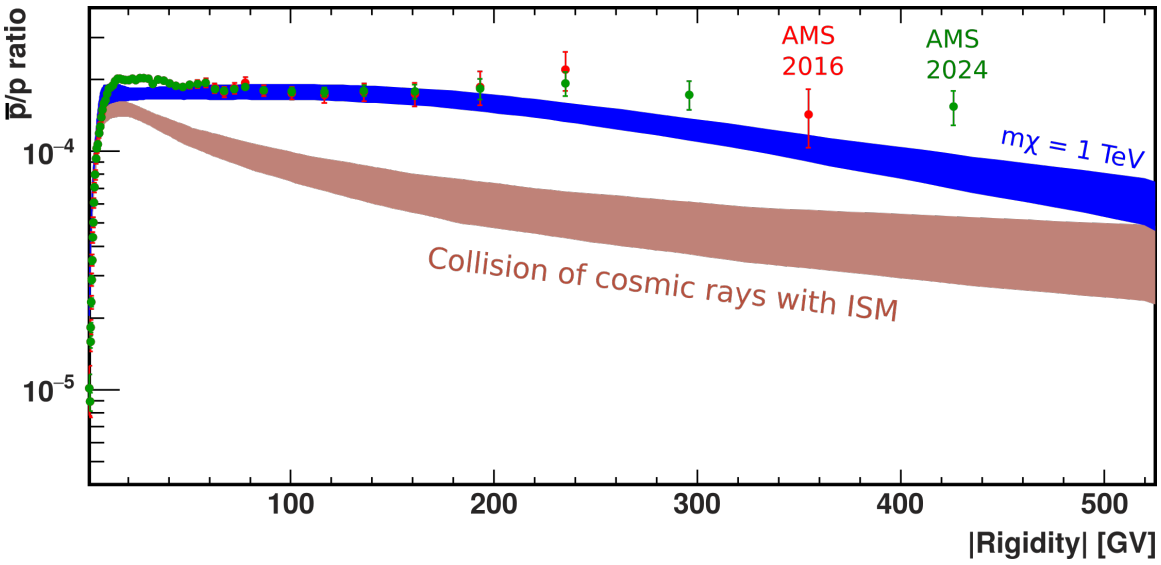

Figure 6-1: The $\bar{p}$/p flux ratio measured in this thesis with AMS. Like the first AMS measurements the observation is not compatible with the pre-AMS expectations based on the production from collision of cosmic rays with the ISM. An extra contribution such as from a dark matter model [68], shown here with the $m_\chi = 1$ TeV, is needed. With continued measurements AMS will resolve between different possible sources of this discrepancy. The projection of the AMS 2024 measurement is based on the minimal Equation (5.1) fit above 60.3 GV.

6.2 Search for heavy antimatter

The fluxes of all the elementary particle in cosmic rays including the antimatter component (e^+ and $\bar{p}$) has been presented. Observation of other heavier antimatter such as anti-deuterium, anti-helium , or even anti-carbon could be important clues to the nature of baryogenesis and dark matter [128, 129].

Such an observation is also possible for AMS, although such a measurement presents an enormous challenge. For example, anti-helium may present only a few candidates per year on a background of 3.7 billion helium events already observed

[26].

Together, such rare event searches, combined with improving the precision of the results presented here leaves enormous new physics potential for AMS. Capturing this potential will require taking advantage of the AMS long exposure time, large acceptance, and an even more detailed understanding of the detector.

Appendix A

Table of results

This table lists the ($\bar{\mathrm{p}}$/p) flux ratio, $\Phi^{\bar{p}}/\Phi^{p}$, and the $\bar{\mathrm{p}}$ flux, $\Phi^{\bar{p}}$. The results are shown as a function of absolute rigidity, $|R|$, at the top of AMS. Also shown are $\tilde{N}^{\bar{p}}$, the number of antiprotons in each rigidity bin, σ_{stat}, the statistical error on the flux ratio, $\sigma^{A}_{\mathrm{syst}}$, the systematic error due to the folded acceptance ratio $\tilde{A}^{p}/\tilde{A\bar{p}}$, $\sigma^{N}_{\mathrm{syst}}$, the systematic error due to the ratio of the number of selected events $\tilde{N}^{\bar{p}}_{i}/\tilde{N}^{p}_{i}$, $\sigma^{R}_{\mathrm{syst}}$, the systematic error on the rigidity scale, and σ_{syst}, the total systematic error on the flux ratio. $\Phi^{\bar{p}}$ is in units of $[\mathrm{m}^2\,\mathrm{sr\,s\,GV}]^{-1}$. For $\Phi^{\bar{p}}$, σ^{Φ}_{stat} is the statistical error and σ^{Φ}_{syst} is the systematic error.

$\lvert R\rvert$ [GV]	$\tilde{N}_{\bar{\mathrm{p}}}$	$\Phi^{\bar{p}}/\Phi^{\mathrm{p}}$ σ_{stat} σ^{N}_{syst} σ^{A}_{syst} σ^{R}_{syst} σ_{syst}	$\Phi^{\bar{p}}$ σ^{Φ}_{stat} σ^{Φ}_{syst}
1.00 – 1.16	21	(1.017 0.225 0.069 0.047 0.000 0.083)$\times10^{-5}$	(5.945 1.315 0.578)$\times10^{-3}$
1.16 – 1.33	74	(8.934 1.090 0.523 0.406 0.002 0.662)$\times10^{-6}$	(5.575 0.680 0.505)$\times10^{-3}$
1.33 – 1.51	233	(1.588 0.110 0.051 0.071 0.000 0.088)$\times10^{-5}$	(9.750 0.677 0.676)$\times10^{-3}$
1.51 – 1.71	502	(1.827 0.092 0.047 0.081 0.001 0.093)$\times10^{-5}$	(1.063 0.054 0.068)$\times10^{-2}$
1.71 – 1.92	888	(2.327 0.096 0.056 0.101 0.001 0.116)$\times10^{-5}$	(1.249 0.051 0.077)$\times10^{-2}$
1.92 – 2.15	1449	(2.896 0.101 0.069 0.124 0.001 0.142)$\times10^{-5}$	(1.401 0.049 0.084)$\times10^{-2}$
2.15 – 2.40	2192	(3.496 0.107 0.075 0.148 0.001 0.166)$\times10^{-5}$	(1.500 0.046 0.087)$\times10^{-2}$
2.40 – 2.67	3366	(4.360 0.113 0.079 0.183 0.001 0.199)$\times10^{-5}$	(1.638 0.043 0.092)$\times10^{-2}$
2.67 – 2.97	4474	(5.046 0.122 0.087 0.209 0.001 0.227)$\times10^{-5}$	(1.639 0.040 0.090)$\times10^{-2}$
2.97 – 3.29	6028	(6.072 0.127 0.099 0.249 0.002 0.267)$\times10^{-5}$	(1.690 0.035 0.090)$\times10^{-2}$
3.29 – 3.64	7321	(7.050 0.138 0.097 0.285 0.002 0.301)$\times10^{-5}$	(1.668 0.033 0.087)$\times10^{-2}$
3.64 – 4.02	8592	(7.964 0.146 0.064 0.317 0.002 0.323)$\times10^{-5}$	(1.588 0.029 0.079)$\times10^{-2}$

Continued on next page ...

$\|R\|$ [GV]	$\tilde{N}_{\bar{\mathrm{p}}}$	$\Phi^{\bar{p}}/\Phi^{\mathrm{p}}$	σ_{stat}	σ^{N}_{syst}	σ^{A}_{syst}	σ^{R}_{syst}	σ_{syst}	$\Phi^{\bar{p}}$	σ^{Φ}_{stat}	σ^{Φ}_{syst}
4.02 – 4.43	1932	$(9.310$	0.212	0.081	0.366	0.002	$0.375)\times10^{-5}$	$(1.557$	0.035	$0.076)\times10^{-2}$
4.43 – 4.88	3083	$(1.028$	0.019	0.008	0.040	0.000	$0.041)\times10^{-4}$	$(1.432$	0.026	$0.069)\times10^{-2}$
4.88 – 5.37	3880	$(1.070$	0.017	0.003	0.041	0.000	$0.041)\times10^{-4}$	$(1.230$	0.020	$0.058)\times10^{-2}$
5.37 – 5.90	4780	$(1.189$	0.017	0.004	0.045	0.000	$0.045)\times10^{-4}$	$(1.121$	0.016	$0.052)\times10^{-2}$
5.90 – 6.47	5472	$(1.272$	0.017	0.004	0.048	0.000	$0.048)\times10^{-4}$	$(9.798$	0.133	$0.449)\times10^{-3}$
6.47 – 7.09	6538	$(1.385$	0.017	0.004	0.051	0.000	$0.052)\times10^{-4}$	$(8.686$	0.109	$0.392)\times10^{-3}$
7.09 – 7.76	7369	$(1.492$	0.018	0.006	0.055	0.000	$0.055)\times10^{-4}$	$(7.588$	0.090	$0.338)\times10^{-3}$
7.76 – 8.48	7818	$(1.589$	0.018	0.009	0.057	0.000	$0.058)\times10^{-4}$	$(6.545$	0.076	$0.289)\times10^{-3}$
8.48 – 9.26	7821	$(1.642$	0.019	0.010	0.059	0.000	$0.060)\times10^{-4}$	$(5.462$	0.063	$0.239)\times10^{-3}$
9.26 – 10.1	20,382	$(1.740$	0.012	0.012	0.062	0.000	$0.063)\times10^{-4}$	$(4.669$	0.033	$0.202)\times10^{-3}$
10.1 – 11.0	19,445	$(1.829$	0.013	0.013	0.064	0.001	$0.065)\times10^{-4}$	$(3.956$	0.029	$0.168)\times10^{-3}$
11.0 – 12.0	18,769	$(1.857$	0.014	0.013	0.064	0.001	$0.066)\times10^{-4}$	$(3.228$	0.024	$0.136)\times10^{-3}$
12.0 – 13.0	16,372	$(1.890$	0.015	0.015	0.065	0.001	$0.066)\times10^{-4}$	$(2.650$	0.021	$0.111)\times10^{-3}$
13.0 – 14.1	16,076	$(1.964$	0.016	0.015	0.067	0.001	$0.068)\times10^{-4}$	$(2.234$	0.018	$0.093)\times10^{-3}$
14.1 – 15.3	15,578	$(2.018$	0.017	0.025	0.067	0.001	$0.072)\times10^{-4}$	$(1.853$	0.015	$0.078)\times10^{-3}$
15.3 – 16.6	14,734	$(2.017$	0.017	0.025	0.066	0.001	$0.071)\times10^{-4}$	$(1.492$	0.013	$0.062)\times10^{-3}$
16.6 – 18.0	15,816	$(2.001$	0.017	0.018	0.064	0.002	$0.066)\times10^{-4}$	$(1.191$	0.010	$0.047)\times10^{-3}$
18.0 – 19.5	15,049	$(1.987$	0.017	0.017	0.061	0.002	$0.063)\times10^{-4}$	$(9.533$	0.082	$0.368)\times10^{-4}$
19.5 – 21.1	14,426	$(1.993$	0.018	0.018	0.058	0.002	$0.061)\times10^{-4}$	$(7.724$	0.069	$0.289)\times10^{-4}$
21.1 – 22.8	13,511	$(2.018$	0.019	0.018	0.056	0.002	$0.059)\times10^{-4}$	$(6.326$	0.058	$0.229)\times10^{-4}$
22.8 – 24.7	12,943	$(1.986$	0.019	0.018	0.053	0.003	$0.056)\times10^{-4}$	$(5.022$	0.047	$0.176)\times10^{-4}$
24.7 – 26.7	11,723	$(2.021$	0.020	0.019	0.050	0.003	$0.054)\times10^{-4}$	$(4.112$	0.041	$0.139)\times10^{-4}$
26.7 – 28.8	10,411	$(2.020$	0.021	0.019	0.047	0.003	$0.051)\times10^{-4}$	$(3.323$	0.035	$0.108)\times10^{-4}$
28.8 – 31.1	9508	$(2.016$	0.023	0.021	0.044	0.004	$0.049)\times10^{-4}$	$(2.682$	0.030	$0.084)\times10^{-4}$
31.1 – 33.5	7876	$(1.919$	0.024	0.021	0.039	0.004	$0.044)\times10^{-4}$	$(2.067$	0.026	$0.063)\times10^{-4}$
33.5 – 36.1	7212	$(2.003$	0.027	0.024	0.041	0.005	$0.047)\times10^{-4}$	$(1.750$	0.023	$0.053)\times10^{-4}$
36.1 – 38.9	6127	$(1.984$	0.029	0.025	0.040	0.005	$0.048)\times10^{-4}$	$(1.405$	0.021	$0.043)\times10^{-4}$
38.9 – 41.9	2697	$(1.921$	0.041	0.026	0.039	0.005	$0.047)\times10^{-4}$	$(1.103$	0.023	$0.034)\times10^{-4}$
41.9 – 45.1	2353	$(1.883$	0.043	0.027	0.038	0.005	$0.047)\times10^{-4}$	$(8.778$	0.200	$0.260)\times10^{-5}$
45.1 – 48.5	1962	$(1.858$	0.047	0.029	0.038	0.006	$0.048)\times10^{-4}$	$(7.046$	0.177	$0.208)\times10^{-5}$
48.5 – 52.2	1772	$(1.908$	0.051	0.032	0.039	0.006	$0.051)\times10^{-4}$	$(5.892$	0.157	$0.174)\times10^{-5}$
52.2 – 56.1	1528	$(1.913$	0.056	0.033	0.039	0.007	$0.051)\times10^{-4}$	$(4.817$	0.140	$0.143)\times10^{-5}$
56.1 – 60.3	1300	$(1.938$	0.062	0.038	0.039	0.007	$0.055)\times10^{-4}$	$(3.988$	0.127	$0.124)\times10^{-5}$
60.3 – 64.8	1143	$(1.837$	0.065	0.041	0.037	0.008	$0.056)\times10^{-4}$	$(3.088$	0.109	$0.102)\times10^{-5}$

Continued on next page . . .

$\|R\|$ [GV]	$\tilde{N}_{\bar{\mathrm{p}}}$	$\Phi^{\bar{p}}/\Phi^{\mathrm{p}}$	σ_{stat}	σ^{N}_{syst}	σ^{A}_{syst}	σ^{R}_{syst}	σ_{syst}	$\Phi^{\bar{p}}$	σ^{Φ}_{stat}	σ^{Φ}_{syst}
64.8 – 69.7	1002	$(1.773$	0.068	0.043	0.036	0.008	$0.057)\times10^{-4}$	$(2.432$	0.094	$0.083)\times10^{-5}$
69.7 – 74.9	916	$(1.838$	0.075	0.050	0.037	0.010	$0.063)\times10^{-4}$	$(2.060$	0.084	$0.075)\times10^{-5}$
74.9 – 80.5	841	$(1.940$	0.084	0.056	0.039	0.010	$0.069)\times10^{-4}$	$(1.778$	0.077	$0.067)\times10^{-5}$
80.5 – 93.0	1270	$(1.796$	0.066	0.053	0.036	0.010	$0.065)\times10^{-4}$	$(1.217$	0.045	$0.048)\times10^{-5}$
93.0 – 108	980	$(1.752$	0.078	0.060	0.036	0.011	$0.070)\times10^{-4}$	$(7.863$	0.351	$0.338)\times10^{-6}$
108 – 125	733	$(1.720$	0.099	0.065	0.035	0.013	$0.075)\times10^{-4}$	$(5.091$	0.293	$0.236)\times10^{-6}$
125 – 147	573	$(1.770$	0.124	0.074	0.036	0.016	$0.084)\times10^{-4}$	$(3.393$	0.237	$0.169)\times10^{-6}$
147 – 175	223	$(1.743$	0.172	0.087	0.035	0.017	$0.095)\times10^{-4}$	$(2.077$	0.205	$0.119)\times10^{-6}$
175 – 211	83	$(1.860$	0.261	0.145	0.038	0.022	$0.152)\times10^{-4}$	$(1.332$	0.187	$0.111)\times10^{-6}$
211 – 259	72	$(2.201$	0.344	0.215	0.045	0.030	$0.222)\times10^{-4}$	$(9.113$	1.424	$0.931)\times10^{-7}$
259 – 450	66	$(1.426$	0.341	0.187	0.029	0.027	$0.191)\times10^{-4}$	$(2.126$	0.509	$0.287)\times10^{-7}$

List of Figures

Bibliography

[1] M. Aguilar, *et al.* (AMS Collaboration), Physics Reports **366**, 331 (2002).

[2] M. Aguilar, *et al.* (AMS Collaboration), Physical Review Letters **117**, 091103 (2016).

[3] A. I. Chen, in *Proceedings of Science* (38th International Conference on High Energy Physics, Chicago, USA, 2016).

[4] M. S. Turner and F. Wilczek, Physical Review D **42**, 1001 (1990).

[5] J. Ellis, 26th International Cosmic Ray Conference, ICRC XXVI **516**, 21 (2000).

[6] L. J. Watson, D. J. Mortlock, and A. H. Jaffe, Monthly Notices of the Royal Astronomical Society **418**, 206 (2011).

[7] E. Fermi, Physical Review **75**, 1169 (1949).

[8] I. V. Moskalenko and A. W. Strong, The Astrophysical Journal **493**, 694 (1998).

[9] A. W. Strong, I. V. Moskalenko, and V. S. Ptuskin, Annual Review of Nuclear and Particle Science **57**, 285 (2007).

[10] V. S. Ptuskin, I. V. Moskalenko, F. C. Jones, A. W. Strong, and V. N. Zirakashvili, The Astrophysical Journal **642**, 902 (2006).

[11] V. Ptuskin, Astroparticle Physics **39-40**, 44 (2012).

[12] L. F. Burlaga, N. F. Ness, and M. H. Acuña, The Astrophysical Journal **642**, 584 (2006).

[13] T. Porter and R. Protheroe, Journal of Physics G Nuclear Physics **23**, 1765 (1997).

[14] D. E. Dorfan, J. Eades, L. M. Lederman, W. Lee, and S. C. C. Ting, Physical Review Letters **14**, 1003 (1965).

[15] H. Agakishiev *et al.* (STAR), Nature **473**, 353 (2011).

[16] V. L. Ginzburg and V. S. Ptuskin, Soviet Physics Uspekhi **18**, 931 (1975).

[17] V. S. Ptuskin, F. C. Jones, and J. F. Ormes, The Astrophysical Journal **465**, 972 (1996).

[18] M. Boezio, *et al.*, Astroparticle Physics **19**, 583 (2003).

[19] F. Aversa, *et al.*, International Cosmic Ray Conference **3**, 9 (1995).

[20] S. Barwick, *et al.*, The Astrophysical Journal **482**, L191 (1997).

[21] M. Aguilar, *et al.* (AMS Collaboration), Physical Review Letters **110**, 141102 (2013).

[22] L. Accardo, *et al.* (AMS Collaboration), Physical Review Letters **113**, 121101 (2014).

[23] M. Aguilar, *et al.* (AMS Collaboration), Physical Review Letters **113**, 121102 (2014).

[24] M. Aguilar, *et al.* (AMS Collaboration), Physical Review Letters **113**, 221102 (2014).

[25] M. Aguilar, *et al.* (AMS Collaboration), Physical Review Letters **114**, 171103 (2015).

[26] M. Aguilar, *et al.* (AMS Collaboration), Physical Review Letters **115**, 211101 (2015).

[27] M. Aguilar, *et al.* (AMS Collaboration), Physical Review Letters **117**, 231102 (2016).

[28] J. Kopp, Physical Review D **88**, 076013 (2013).

[29] M. Drees and G. Gerbier, ArXiv e-prints (2012), 1204.2373 [hep-ph] .

[30] Planck Collaboration, *et al.*, Astronomy & Astrophysics **594**, A13 (2016).

[31] W. H. Press and P. Schechter, The Astrophysical Journal **187**, 425 (1974).

[32] G. A. Dooley, *et al.*, The Astrophysical Journal **786**, 50 (2014).

[33] P. Mertsch and S. Sarkar, Physical Review D **90**, 061301 (2014).

[34] P. Blasi and P. D. Serpico, Physical Review Letters **103**, 081103 (2009).

[35] Y. Fujita, K. Kohri, R. Yamazaki, and K. Ioka, Physical Review D **80**, 063003 (2009).

[36] K. Kohri, K. Ioka, Y. Fujita, and R. Yamazaki, Progress of Theoretical and Experimental Physics **2016**, 021E01 (2016).

[37] I. Cholis and D. Hooper, Physical Review D **88**, 023013 (2013).

[38] T. Linden and S. Profumo, The Astrophysical Journal **772**, 18 (2013).

[39] K. Blum, B. Katz, and E. Waxman, Physical Review Letters **111**, 211101 (2013).

[40] R. Cowsik, B. Burch, and T. Madziwa-Nussinov, The Astrophysical Journal **786**, 124 (2014).

[41] R. Kappl and M. W. Winkler, Journal of Cosmology and Astroparticle Physics **9**, 051 (2014).

[42] H. B. Jin, Y. L. Wu, and Y. F. Zhou, Physical Review D **92**, 055027 (2015).

[43] L. Bergström, T. Bringmann, I. Cholis, D. Hooper, and C. Weniger, Physical Review Letters **111**, 171101 (2013).

[44] C. H. Chen, C. W. Chiang, and T. Nomura, Physics Letters B **747**, 495 (2015).

[45] M. S. Madhavacheril, N. Sehgal, and T. R. Slatyer, Physical Review D **89**, 103508 (2014).

[46] V. A. Mitsou, International Journal of Modern Physics A **28**, 1330052 (2013).

[47] R. Agnese *et al.* (CDMS), Physical Review Letters **111**, 251301 (2013).

[48] S. Chatrchyan, *et al.*, Physics Letters B **716**, 30 (2012).

[49] G. Aad, *et al.*, Physics Letters B **716**, 1 (2012).

[50] M. Cirelli, *et al.*, Journal of Cosmology and Astroparticle Physics **2011**, 051 (2011).

[51] R. L. Golden, *et al.*, Physical Review Letters **43**, 1196 (1979).

[52] A. Buffington and S. M. Schindler, The Astrophysical Journal **247**, L105 (1981).

[53] K. Yoshimura, *et al.*, Physical Review Letters **75**, 3792 (1995).

[54] S. Orito, *et al.*, Physical Review Letters **84**, 1078 (2000).

[55] Y. Asaoka, *et al.*, Physical Review Letters **88**, 051101 (2002).

[56] K. Abe, *et al.*, Physics Letters B **670**, 103 (2008).

[57] K. Abe, *et al.*, Physical Review Letters **108**, 051102 (2012).

[58] K. Abe, *et al.*, The Astrophysical Journal **822**, 65 (2016).

[59] M. Boezio, *et al.*, The Astrophysical Journal **487**, 415 (1997).

[60] M. Boezio, *et al.*, The Astrophysical Journal **561**, 787 (2001).

[61] A. S. Beach, *et al.*, Physical Review Letters **87**, 271101 (2001).

[62] O. Adriani, *et al.* (PAMELA Collaboration), Physical Review Letters **102**, 051101 (2009).

[63] O. Adriani, *et al.*, Physical Review Letters **105**, 121101 (2010).

[64] O. Adriani, *et al.*, JETP Letters **96**, 621 (2013).

[65] C. S. Shen and G. B. Berkey, Physical Review **171**, 1344 (1968).

[66] M. Simon, A. Molnar, and S. Roesler, The Astrophysical Journal **499**, 250 (1998).

[67] I. V. Moskalenko, A. W. Strong, J. F. Ormes, and M. S. Potgieter, The Astrophysical Journal **565**, 280 (2002).

[68] F. Donato, D. Maurin, P. Brun, T. Delahaye, and P. Salati, Physical Review Letters **102**, 071301 (2009).

[69] G. Jungman, M. Kamionkowski, and K. Griest, Physics Reports **267**, 195 (1996).

[70] L. Bergström, Reports on Progress in Physics **63**, 793 (2000).

[71] G. Bertone, D. Hooper, and J. Silk, Physics Reports **405**, 279 (2005).

[72] G. Kane, R. Lu, and S. Watson, Physics Letters B **681**, 151 (2009).

[73] S. W. Hawking, Nature **248**, 30 (1974).

[74] P. Kiraly, J. Szabelski, J. Wdowczyk, and A. W. Wolfendale, Nature **293**, 120 (1981).

[75] A. Kounine, International Journal of Modern Physics E **21**, 1230005 (2012).

[76] S. Ting, Nuclear Physics B **243**, 12 (2013).

[77] R. Battiston, Nuclear Instruments and Methods **588**, 227 (2008), proceedings of the First International Conference on Astroparticle PhysicsRICAP 07.

[78] M. Incagli, AIP Conference Proceedings **1223**, 43 (2010).

[79] S. Rosier-Lees, in *Proceedings of the 19th Symposium on Astroparticle Physics in the Netherlands* (Beekbergen, Netherlands, 2014).

[80] J. Alcaraz, *et al.*, Nuclear Instruments and Methods **A593**, 376 (2008).

[81] P. Zuccon and AMS Tracker Collaboration, Nuclear Instruments and Methods **A596**, 74 (2008).

[82] V. Bindi *et al.*, Nuclear Instruments and Methods **A623**, 968 (2010).

[83] A. Basili, *et al.*, Nuclear Instruments and Methods **A707**, 99 (2013).

[84] P. von Doetinchem, *et al.*, *Proceedings, 11th Topical Seminar on Innovative Particle and Radiation Detectors (IPRD08): Siena, Italy, 1-4 October 2008*, Nucl. Phys. Proc. Suppl. **197**, 15 (2009).

[85] T. Kirn (AMS 02 TRD), *Proceedings, TRDs for the 3rd Millenium: 4th Workshop on Advanced Transition Radiation Detectors for Accelerator and Space Applications (TRD2011): Bari, Italy, September 14-16, 2011*, Nuclear Instruments and Methods **A706**, 43 (2013).

[86] W. Gillard (AMS02-RICH), in *Proceedings, 33rd International Cosmic Ray Conference (ICRC2013): Rio de Janeiro, Brazil, July 2-9, 2013* (2013) p. 0742.

[87] C. Adloff *et al.*, Nuclear Instruments and Methods **A714**, 147 (2013).

[88] G. Ambrosi, *et al.* (AMS Tracker Collaboration), in *Proceedings, 33rd International Cosmic Ray Conference (ICRC2013): Rio de Janeiro, Brazil, July 2-9, 2013* (2013).

[89] G. Ambrosi *et al.*, in *Proceedings, 33rd International Cosmic Ray Conference (ICRC2013): Rio de Janeiro, Brazil, July 2-9, 2013* (2013).

[90] J. Alcaraz, Nuclear Instruments and Methods **553**, 613 (2005).

[91] S. Haino and AMS-02 Tracker Collaboration, Nuclear Instruments and Methods **699**, 221 (2013).

[92] B. P. Roe, *et al.*, Nuclear Instruments and Methods **543**, 577 (2005).

[93] P. Zuccon, Nuclear Physics B **110**, 182 (2002).

[94] Y. T. Yurkin, *et al.*, Bulletin of the Russian Academy of Sciences, Physics **75**, 854 (2011).

[95] J. Alcaraz, *et al.*, Physics Letters B **484**, 10 (2000).

[96] C. Finlay, *et al.*, Geophysical Journal International **183**, 1216 (2010).

[97] E. Thébault, *et al.*, Earth, Planets and Space **67**, 1 (2015).

[98] A. Morselli, in *Frontier Objects in Astrophysics and Particle Physics*, edited by F. Giovannelli and G. Mannocchi (2007) p. 517.

[99] A. Hoecker, *et al.*, ArXiv e-prints (2007), physics/0703039 .

[100] S. Agostinelli, *et al.*, Nuclear Instruments and Methods **506**, 250 (2003).

[101] J. Allison, *et al.*, IEEE Transactions on nuclear science **53**, 270 (2006).

[102] V. Choutko, A. Egorov, A. Eline, and B. S. Shan, in *Journal of Physics Conference Series*, Vol. 664 (2015) p. 032029.

[103] A. Capella, U. Sukhatme, C.-I. Tan, and J. Tran Thanh Van, Physics Reports **236**, 225 (1994).

[104] J. D. Sullivan, Nuclear Instruments and Methods **95**, 5 (1971).

[105] A. Kondor, Nuclear Instruments and Methods **216**, 177 (1983).

[106] G. D'Agostini, Nuclear Instruments and Methods **362**, 487 (1995).

[107] D. F. Smart and M. A. Shea, Advances in Space Research **44**, 1107 (2009).

[108] X. Yan and X. Su, *Linear regression analysis: theory and computing* (World Scientific, 2009).

[109] T. Bowen, M. Di Corato, W. H. Moore, and G. Tagliaferri, Il Nuovo Cimento **9**, 908 (1958).

[110] G. Bellettini, *et al.*, Nuclear Physics **79**, 609 (1966).

[111] S. Denisov, *et al.*, Nuclear Physics B **61**, 62 (1973).

[112] A. Carroll, *et al.*, Physics Letters B **80**, 319 (1979).

[113] N. Abgrall, *et al.* (The NA61/SHINE Collaboration), Physical Review C **84**, 034604 (2011).

[114] B. Cork, G. R. Lambertson, O. Piccioni, and W. A. Wenzel, Physical Review **107**, 248 (1957).

[115] R. J. Abrams, *et al.*, Physical Review D **4**, 3235 (1971).

[116] H. Aihara, *et al.*, Nuclear Physics A **360**, 291 (1981).

[117] K. Nakamura, *et al.*, Physical Review Letters **52**, 731 (1984).

[118] G. Lafferty and T. Wyatt, Nuclear Instruments and Methods **355**, 541 (1995).

[119] A. D. Erlykin and A. W. Wolfendale, Journal of Physics G Nuclear Physics **43**, 105201 (2016).

[120] M. Duerr, *et al.*, *Hunting the dark Higgs* (2017) arXiv:1701.08780 [hep-ph] .

[121] M. Stref and J. Lavalle, Physical Review D **95**, 063003 (2017).

[122] Oscar Catà, Alejandro Ibarra, and Sebastian Ingenhütt, Physical Review D **95**, 035011 (2017).

[123] A. Cuoco, M. Krämer, and M. Korsmeier, *Novel dark matter constraints from antiprotons in the light of AMS-02* (2016) arXiv:1610.03071 [astro-ph.HE] .

[124] B. Khiali, S. Haino, and J. Feng, The Astrophysical Journal **835**, 229 (2017).

[125] A. Kolmogorov, Akademiia Nauk SSSR Doklady **30**, 301 (1941).

[126] J. Feng, N. Tomassetti, and A. Oliva, Physical Review D **94**, 123007 (2016).

[127] Z. Li, C. Delgado, F. Giovacchini, S. Haino, and J. Hoffman, *Antiproton identification below threshold with AMS-02 RICH detector* (2016) arXiv:1611.02301 [physics.ins-det] .

[128] Y. Cui, J. D. Mason, and L. Randall, Journal of High Energy Physics **11**, 17 (2010).

[129] J. Herms, A. Ibarra, A. Vittino, and S. Wild, Journal of Cosmology and Astroparticle Physics **2**, 018 (2017).